



<b>Publication Year</b>	2015
<b>Acceptance in OA @INAF</b>	2020-03-30T12:38:14Z
<b>Title</b>	NuSTAR Spectroscopy of Multi-component X-Ray Reflection from NGC 1068
<b>Authors</b>	Bauer, Franz E.; Arévalo, Patricia; Walton, Dominic J.; Koss, Michael J.; Puccetti, Simonetta; et al.
<b>DOI</b>	10.1088/0004-637X/812/2/116
<b>Handle</b>	<a href="http://hdl.handle.net/20.500.12386/23695">http://hdl.handle.net/20.500.12386/23695</a>
<b>Journal</b>	THE ASTROPHYSICAL JOURNAL
<b>Number</b>	812

*NuSTAR* SPECTROSCOPY OF MULTI-COMPONENT X-RAY REFLECTION FROM NGC 1068

FRANZ E. BAUER<sup>1,2,3,4</sup>, PATRICIA ARÉVALO<sup>3,5</sup>, DOMINIC J. WALTON<sup>6,7</sup>, MICHAEL J. KOSS<sup>8,26</sup>, SIMONETTA PUCETTI<sup>9,10</sup>,  
 POSHAK GANDHI<sup>11</sup>, DANIEL STERN<sup>7</sup>, DAVID M. ALEXANDER<sup>12</sup>, MISLAV BALOKOVIĆ<sup>6</sup>, STEVE E. BOGGS<sup>13</sup>, WILLIAM N. BRANDT<sup>14,15</sup>,  
 MURRAY BRIGHTMAN<sup>6</sup>, FINN E. CHRISTENSEN<sup>16</sup>, ANDREA COMASTRI<sup>17</sup>, WILLIAM W. CRAIG<sup>13,18</sup>, AGNESE DEL MORO<sup>12</sup>,  
 CHARLES J. HAILEY<sup>19</sup>, FIONA A. HARRISON<sup>6</sup>, RYAN HICKOX<sup>20</sup>, BIN LUO<sup>14</sup>, CRAIG B. MARKWARDT<sup>21</sup>, ANDREA MARINUCCI<sup>22</sup>,  
 GIORGIO MATT<sup>22</sup>, JANE R. RIGBY<sup>21</sup>, ELIZABETH RIVERS<sup>6</sup>, CRISTIAN SAEZ<sup>23</sup>, EZEQUIEL TREISTER<sup>3,24</sup>, C. MEGAN URRY<sup>25</sup>,  
 AND WILLIAM W. ZHANG<sup>21</sup>

<sup>1</sup> Pontificia Universidad Católica de Chile, Instituto de Astrofísica, Casilla 306, Santiago 22, Chile

<sup>2</sup> Millenium Institute of Astrophysics, Santiago, Chile

<sup>3</sup> EMBIGGEN Anillo, Concepción, Chile

<sup>4</sup> Space Science Institute, 4750 Walnut Street, Suite 205, Boulder, CO 80301, USA

<sup>5</sup> Instituto de Física y Astronomía, Facultad de Ciencias, Universidad de Valparaíso, Gran Bretaña N 1111, Playa Ancha, Valparaíso, Chile

<sup>6</sup> Cahill Center for Astronomy and Astrophysics, California Institute of Technology, Pasadena, CA 91125, USA

<sup>7</sup> Jet Propulsion Laboratory, California Institute of Technology, 4800 Oak Grove Drive, Pasadena, CA 91109, USA

<sup>8</sup> Institute for Astronomy, Department of Physics, ETH Zurich, Wolfgang-Pauli-Strasse 27, CH-8093 Zurich, Switzerland

<sup>9</sup> ASDC-ASI, Via del Politecnico, I-00133 Roma, Italy

<sup>10</sup> INAF-Osservatorio Astronomico di Roma, via Frascati 33, I-00040 Monte Porzio Catone (RM), Italy

<sup>11</sup> School of Physics and Astronomy, University of Southampton, Highfield, Southampton SO17 1BJ, UK

<sup>12</sup> Department of Physics, Durham University, South Road, Durham, DH1 3LE, UK

<sup>13</sup> Space Sciences Laboratory, University of California, Berkeley, CA 94720, USA

<sup>14</sup> Department of Astronomy and Astrophysics, The Pennsylvania State University, 525 Davey Lab, University Park, PA 16802, USA

<sup>15</sup> Institute for Gravitation and the Cosmos, The Pennsylvania State University, University Park, PA 16802, USA

<sup>16</sup> DTU Space, National Space Institute, Technical University of Denmark, Elektrovej 327, DK-2800 Lyngby, Denmark

<sup>17</sup> INAF-Osservatorio Astronomico di Bologna, via Ranzani 1, I-40127 Bologna, Italy

<sup>18</sup> Lawrence Livermore National Laboratory, Livermore, CA 945503, USA

<sup>19</sup> Columbia Astrophysics Laboratory, Columbia University, New York, NY 10027, USA

<sup>20</sup> Department of Physics and Astronomy, Dartmouth College, 6127 Wilder Laboratory, Hanover, NH 03755, USA

<sup>21</sup> NASA Goddard Space Flight Center, Greenbelt, MD 20771, USA

<sup>22</sup> Dipartimento di Matematica e Fisica, Università degli Studi Roma Tre, via della Vasca Navale 84, I-00146 Roma, Italy

<sup>23</sup> Department of Astronomy, University of Maryland, College Park, MD 20742, USA

<sup>24</sup> Departamento de Astronomía Universidad de Concepción, Casilla 160-C, Concepción, Chile

<sup>25</sup> Department of Physics and Yale Center for Astronomy and Astrophysics, Yale University, New Haven, CT 06520-8120, USA

Received 2014 November 3; accepted 2015 September 8; published 2015 October 14

## ABSTRACT

We report on high-energy X-ray observations of the Compton-thick Seyfert 2 galaxy NGC 1068 with *NuSTAR*, which provide the best constraints to date on its  $>10$  keV spectral shape. The *NuSTAR* data are consistent with those from past and current instruments to within cross-calibration uncertainties, and we find no strong continuum or line variability over the past two decades, which is in line with its X-ray classification as a reflection-dominated Compton-thick active galactic nucleus. The combined *NuSTAR*, *Chandra*, *XMM-Newton*, and *Swift* BAT spectral data set offers new insights into the complex secondary emission seen instead of the completely obscured transmitted nuclear continuum. The critical combination of the high signal-to-noise *NuSTAR* data and the decomposition of the nuclear and extranuclear emission with *Chandra* allow us to break several model degeneracies and greatly aid physical interpretation. When modeled as a monolithic (i.e., a single  $N_{\text{H}}$ ) reflector, none of the common Compton reflection models are able to match the neutral fluorescence lines and broad spectral shape of the Compton reflection hump without requiring unrealistic physical parameters (e.g., large Fe overabundances, inconsistent viewing angles, or poor fits to the spatially resolved spectra). A multi-component reflector with three distinct column densities (e.g., with best-fit values of  $N_{\text{H}}$  of  $1.4 \times 10^{23}$ ,  $5.0 \times 10^{24}$ , and  $10^{25} \text{ cm}^{-2}$ ) provides a more reasonable fit to the spectral lines and Compton hump, with near-solar Fe abundances. In this model, the higher  $N_{\text{H}}$  component provides the bulk of the flux to the Compton hump, while the lower  $N_{\text{H}}$  component produces much of the line emission, effectively decoupling two key features of Compton reflection. We find that  $\approx 30\%$  of the neutral Fe  $K\alpha$  line flux arises from  $>2''$  ( $\approx 140$  pc) and is clearly extended, implying that a significant fraction (and perhaps most) of the  $<10$  keV reflected component arises from regions well outside a parsec-scale torus. These results likely have ramifications for the interpretation of Compton-thick spectra from observations with poorer signal-to-noise and/or more distant objects.

*Key words:* galaxies: active – galaxies: individual (NGC 1068) – X-rays: galaxies

<sup>26</sup> SNSF Ambizione Postdoctoral Fellow.

## 1. INTRODUCTION

At a distance of  $\approx 14.4$  Mpc (Tully 1988), NGC 1068 is one of the nearest and best-studied active galactic nuclei (AGN). It is traditionally classified as a Seyfert 2 galaxy, and was the first type 2 AGN observed to possess polarized optical broad line emission; these broad line regions (BLRs) seen only in scattered light are presumably obscured by a dusty edge-on structure (a.k.a., the “torus”; Antonucci & Miller 1985; Miller et al. 1991), thereby establishing the standard orientation-based model of AGN unification as we know it today (Antonucci 1993; Urry & Padovani 1995). NGC 1068 has continued to be an exceptionally rich source for studying AGN in general, and Compton-thick AGN in particular,<sup>27</sup> with spatially resolved studies of its AGN structure down to  $\approx 0.5$ –70 pc over many critical portions of the electromagnetic spectrum ( $1'' = 70$  pc at the distance of NGC 1068). In many ways, NGC 1068 is considered an archetype of an obscured AGN.

In terms of its basic properties and structure, nuclear  $\text{H}_2\text{O}$  megamaser emission associated with a thin disk constrain the supermassive black hole (SMBH) mass at the center of NGC 1068 to  $\approx 1 \times 10^7 M_\odot$  within 0.65 pc, although the observed deviations from Keplerian rotation leave some ambiguity about the overall mass distribution (e.g., Greenhill et al. 1996; Lodato & Bertin 2003; Gallimore et al. 2004). A dynamical virial mass estimate based on the width of the polarized broad  $\text{H}_\beta$  line,  $\sigma_{\text{H}\beta}$ , from scattered light in the hidden BLR finds a consistent mass of  $(9.0 \pm 6.6) \times 10^6 M_\odot$  (e.g., Kuo et al. 2011). NGC 1068’s bolometric luminosity is estimated to be  $L_{\text{bol}} = (6\text{--}10) \times 10^{44} \text{ erg s}^{-1}$  (Woo & Urry 2002; Alonso-Herrero et al. 2011) based on mid-infrared (MIR) spectral modeling, assuming reprocessed AGN emission. Combined with the SMBH mass estimate, this luminosity approaches  $\approx 50\%$ – $80\%$  of the Eddington luminosity, indicating rapid accretion.

Very Long Baseline Interferometry (VLBI) observations of the maser disk constrain it to lie between the radii of 0.6–1.1 pc at a position angle (PA) of  $\approx -45^\circ$  (east of north; e.g., Greenhill et al. 1996). At centimeter wavelengths, a weak kpc-scale, steep-spectrum radio jet is seen to extend out from the nucleus, initially at  $\text{PA} = 12^\circ$  before bending to  $\text{PA} = 30^\circ$  at large scales (e.g., Wilson & Ulvestad 1987; Gallimore et al. 1996). Fainter radio structures close to the nucleus are also observed to trace both the maser disk and an inner X-ray-irradiated molecular disk extending out to  $\approx 0.4$  pc with a  $\text{PA} \approx -60^\circ$  (e.g., Gallimore et al. 2004).

At MIR wavelengths, a complex obscuring structure has been spatially resolved in NGC 1068 via Keck and Very Large Telescope (VLT) interferometry (e.g., Bock et al. 2000; Jaffe et al. 2004), and appears to comprise at least two distinct components (Raban et al. 2009; Schartmann et al. 2010). The first is a  $\sim 800$  K, geometrically thin, disk-like structure extending  $\approx 1.35$  pc by 0.45 pc in size (full-width half maximum, FWHM) and aligned at  $\text{PA} = -42^\circ$ , which is likely associated with the maser disk. The second is a  $\sim 300$  K, more flocculent, filamentary, torus-like distribution  $\approx 3$ –4 pc in size (FWHM), which has been identified with the traditional torus. Spectral modeling of the overall MIR light suggests a torus radius of  $\approx 2$  pc and angular width of  $26_{-4}^{+6}$  deg, a viewing angle of  $88_{-3}^{+2}$  deg with respect to the line of sight, and a

covering factor of  $\approx 25\%$ – $40\%$  (Alonso-Herrero et al. 2011). While no dust reverberation studies have been published on NGC 1068, the sizes from interferometry are consistent with the inner radii determined from dust reverberation studies of type 1 AGN (Suganuma et al. 2006; Koshida et al. 2014).

NGC 1068 also displays a striking extended narrow-line region (NLR) that is roughly co-spatial with the radio jet and lobe emission (e.g., Wilson & Ulvestad 1987). The NLR has been extensively characterized by narrow-band imaging and IFU studies (Evans et al. 1991; Macchetto et al. 1994; Capetti et al. 1997; Veilleux et al. 2003). The biconical ionization cone has been observed out to radii of  $\gtrsim 150''$ , with an apparent opening angle of  $\approx 60^\circ$  centered at  $\text{PA} \approx 35^\circ$ – $45^\circ$  (Unger et al. 1992; Veilleux et al. 2003). The narrow-line emitting clouds are part of a large-scale, radiatively accelerated outflow with velocities up to  $\approx 3200 \text{ km s}^{-1}$  (e.g., Cecil et al. 1990, 2002; Crenshaw & Kraemer 2000). The morphology of the NLR seems to primarily trace the edges of the radio lobe, suggesting that the radio outflow has swept up and compressed the interstellar gas, giving rise to enhanced line-emitting regions. The energetics of the line emission indicate that it is probably photoionization dominated (Dopita et al. 2002; Groves et al. 2004). Various studies have reported strongly non-solar abundances in the ionized gas of NGC 1068, which either require large over- or underabundances of some elements (e.g., due to shocks; supernovae pollution of Ni, P, and similar; or that elements like C and Fe are predominantly locked in dust grains; Kraemer et al. 1998; Oliva et al. 2001; Martins et al. 2010), or can also be explained by multi-component photoionization models with varying densities (e.g., Kraemer & Crenshaw 2000; Kraemer et al. 2015, hereafter K15).

As we now know, the primary AGN continuum of NGC 1068 from the optical to X-rays is completely obscured along our line of sight due to the relative orientations of the disk and obscuring torus, which has a column density  $N_{\text{H}} > 10^{25} \text{ cm}^{-2}$  (e.g., Matt et al. 2000). Thus, the only X-ray emission that we see is scattered into our line of sight. Past observations have suggested that there are two “reflectors” that contribute to the X-ray spectrum (e.g., Matt et al. 1997; Guainazzi et al. 1999). The dominant component is from Compton scattering off the inner “wall” of the neutral obscuring torus, which gives rise to the so-called cold Compton reflection continuum (e.g., Lightman & White 1988). This emission is characterized by a hard X-ray spectral slope with a peak around 30 keV as well as high equivalent-width fluorescent emission lines (e.g., the dominant 6.4 keV iron line; Iwasawa et al. 1997). A second reflector arises from Compton scattering off highly ionized material associated with the ionization cone. The spectral shape of the “warm” reflector is often assumed to crudely mirror the intrinsic continuum, apart from a high-energy cutoff due to Compton down-scattering and potentially significant absorption edges/lines in the spectrum up to a few keV due to various elements, and near  $\sim 7$  keV due to Fe (e.g., Krolik & Kriss 1995). Radiative recombination continuum and line emission (hereafter RRC and RL, respectively) from a broad range of ions and elements can also be observed in relation to the warm reflector, due to photoionization followed by recombination, radiative excitation by absorption of continuum radiation, and inner shell fluorescence (Guainazzi et al. 1999; Brinkman et al. 2002; Kinkhabwala et al. 2002; Ogle et al. 2003; Kallman et al. 2014; hereafter K14; K15). The ionized lines imply observed outflow

<sup>27</sup> With a line of sight column density exceeding  $N_{\text{H}} = 1.5 \times 10^{24} \text{ cm}^{-2}$  and therefore optically thick to Compton scattering.

**Table 1**  
X-Ray Observations

Instrument	Date	Obsid	Exp.	Energy Band	Aperture	Count Rate	Norm Offset
<i>BeppoSAX</i> MECS	1996 Dec 30	5004700100	100.8	3–10	180	0.06	1.13 ± 0.02
<i>BeppoSAX</i> PDS	1996 Dec 30	5004700100	116.6	15–140	...	0.27	0.70 ± 0.10*
<i>BeppoSAX</i> MECS	1998 Jan 11	5004700120	37.3	3–10	180	0.04	1.11 ± 0.02
<i>BeppoSAX</i> PDS	1998 Jan 11	5004700120	31.5	15–140	...	0.28	0.70 ± 0.10*
<i>Chandra</i> ACIS-S	2000 Feb 21	344	47.7	0.4–8	2–75	2.09	1.04 ± 0.04
<i>XMM-Newton</i> pn	2000 Jul 29	0111200101	32.8	0.2–10	75	12.36	1.00
<i>XMM-Newton</i> pn	2000 Jul 30	0111200201	28.7	0.2–10	75	12.36	1.00
<i>Chandra</i> HETG HEG/MEG	2000 Dec 04	332	25.7	0.3–8	2	0.031/0.085	1.09 ± 0.06, 1.05 ± 0.06
<i>Suzaku</i> XIS	2007 Feb 10	701039010	61.5	0.3–9	260	0.73	1.17 ± 0.02
<i>Suzaku</i> HXD PIN	2007 Feb 10	701039010	38.8	15–70	...	0.40	1.20 ± 0.05*
<i>Chandra</i> HETG HEG/MEG	2008 Nov 18	10816	16.2	0.8–10/0.4–8	2	0.029/0.078	1.09 ± 0.06, 1.05 ± 0.06
<i>Chandra</i> HETG HEG/MEG	2008 Nov 19	9149	89.4	0.8–10/0.4–8	2	0.027/0.077	1.09 ± 0.06, 1.05 ± 0.06
<i>Chandra</i> HETG HEG/MEG	2008 Nov 20	10815	19.1	0.8–10/0.4–8	2	0.028/0.076	1.09 ± 0.06, 1.05 ± 0.06
<i>Chandra</i> HETG HEG/MEG	2008 Nov 22	10817	33.2	0.8–10/0.4–8	2	0.028/0.079	1.09 ± 0.06, 1.05 ± 0.06
<i>Chandra</i> HETG HEG/MEG	2008 Nov 25	10823	34.5	0.8–10/0.4–8	2	0.029/0.077	1.09 ± 0.06, 1.05 ± 0.06
<i>Chandra</i> HETG HEG/MEG	2008 Nov 27	9150	41.1	0.8–10/0.4–8	2	0.028/0.077	1.09 ± 0.06, 1.05 ± 0.06
<i>Chandra</i> HETG HEG/MEG	2008 Nov 30	10829	39.6	0.8–10/0.4–8	2	0.027/0.079	1.09 ± 0.06, 1.05 ± 0.06
<i>Chandra</i> HETG HEG/MEG	2008 Dec 03	10830	44.0	0.8–10/0.4–8	2	0.029/0.078	1.09 ± 0.06, 1.05 ± 0.06
<i>Chandra</i> HETG HEG/MEG	2008 Dec 05	9148	80.2	0.8–10/0.4–8	2	0.029/0.078	1.09 ± 0.06, 1.05 ± 0.06
<i>Swift</i> BAT (70-month)	2004–2010	...	9250.0	14–195	...	$4.97 \times 10^{-5}$	0.75 ± 0.10*
<i>NuSTAR</i> FPMA/FPMB	2012 Dec 18	60002030002	56.9/56.8	3–79	75	0.22/0.21	1.11 ± 0.01
<i>Swift</i> XRT	2012 Dec 19	00080252001	2.0	0.5–10	75	0.44	1.13 ± 0.25
<i>NuSTAR</i> FPMA/FPMB	2012 Dec 20	60002030004	47.8/47.5	3–79	75	0.22/0.21	1.11 ± 0.01
<i>NuSTAR</i> FPMA/FPMB	2012 Dec 21	60002030006	19.2/19.4	3–79	75	0.22/0.21	1.11 ± 0.01

**Note.** *Column 1:* satellite and instrument. *Column 2:* starting date of observation. *Column 3:* observation identification (obsid) number. *Chandra* frametimes were  $\approx 1.9$ – $2.1$  s, except for obsids 355, 356, and 2454 with 3.2 s, and obsids 365, 9140, and 10937 with 0.3–0.4 s. *Column 4:* Exposure time in ksec. *Column 5:* energy band in keV. *Column 6:* extraction aperture radius in arcseconds. If a range is given, then an annular region was extracted. For the HETG, the values given represent the half-width of the extraction region in the cross-dispersion direction. *Column 7:* count rate in counts  $s^{-1}$ . *Column 8:* relative normalization offset with respect to the pn in the 3–7 keV band. However, entries denoted by \* are relative to combined *NuSTAR* FPMA/FPMB spectrum in the 20–60 keV band.

velocities of  $400$ – $500$   $km\ s^{-1}$ . Photo-ionized X-ray emission is seen to extend out along the same direction and opening angle as the radio jet/lobe and NLR (Young et al. 2001).

Past observations of NGC 1068 above 10 keV have been limited by available instrumentation, where statistics were dominated by background. Here we report on new observations of NGC 1068 between 3 and 79 keV from *NuSTAR*, whose focusing optics reduce background contamination to unprecedented levels and thus enable a factor of  $\gtrsim 10$  statistical improvement over past observations. The *NuSTAR* data allow the best characterization of the  $>10$  keV spectral shape to date and therefore stand to yield new insights into the nature of Compton-thick obscuration.

This paper is organized as follows: data and reduction methods are briefly detailed in Section 2; X-ray variability analysis is provided in Section 3; X-ray spectroscopic constraints for NGC 1068 are investigated in Section 4, with particular attention to modeling the nucleus and galaxy host contamination; in Section 5 we discuss some implications of the best-fit model; and finally we summarize and explore future prospects in Section 6. We adopt a Galactic neutral column density of  $N_H = 3.0 \times 10^{20}$   $cm^{-2}$  (Kalberla et al. 2005) toward the direction of NGC 1068 and a redshift of 0.00379 (Huchra et al. 1999). Unless stated otherwise, errors on spectral parameters are for 90% confidence, assuming one parameter of interest.

## 2. OBSERVATIONAL DATA AND REDUCTION METHODS

To overcome the limitations of various X-ray instruments in terms of energy coverage and spectral and angular resolution, our strategy was to analyze several high-quality X-ray observations of NGC 1068 obtained by the *NuSTAR*, *Chandra*, and *XMM-Newton* observatories, collected between 2000 and 2013. While *NuSTAR* and *XMM-Newton* have superior collecting areas and energy coverage, neither is able to spatially separate the spectra of the AGN from various sources of host contamination or resolve some line complexes. We therefore use the *Chandra* data for these tasks, which allows us to construct the most robust model to date for the nuclear X-ray spectrum of NGC 1068. We additionally use *Swift*, *Suzaku*, and *BeppoSAX* for points of comparison. The basic parameters of these observations are listed in Table 1. All data were downloaded through the High Energy Astrophysics Science Archive Research Center BROWSE facility.

To account for external cross-calibration discrepancies between observatories, we adopt multiplicative cross-normalization constants. The internal cross-calibration differences for instruments in the same energy range are generally known to be within  $\sim 5\%$  of unity for all such missions, while cross-calibration differences, both for instruments with widely different energy ranges and between instruments from different observatories, can be as high as  $\sim 30\%$  (see Table 1). The final

spectra have all been binned to contain a minimum of 25 counts per bin, sufficient for  $\chi^2$  minimization.

### 2.1. *NuSTAR*

The *NuSTAR* observatory is the first focusing satellite with sensitivity over the broad 3–79 keV energy band (Harrison et al. 2013). It consists of two co-aligned X-ray optics/detector pairs, with corresponding focal plane modules FPMA and FPMB, which offer a  $12'5 \times 12'5$  field of view (FOV), angular resolutions of  $18''$  Full Width Half Max (FWHM) and  $1'$  Half Power Diameter (HPD) over the 3–79 keV X-ray band, and a characteristic spectral resolution of 400 eV (FWHM) at 10 keV. NGC 1068 was observed by *NuSTAR* on 2012 December 18–21.

The *NuSTAR* data were processed using the standard pipeline (NUPipeline; Perri et al. 2014) from the *NuSTAR* Data Analysis Software (v1.3.0) within the HEASoft package (v6.15), in combination with CALDB v20131007. The unfiltered event lists were screened to reduce internal background at high energies via standard depth corrections and remove South Atlantic Anomaly (SAA) passages. The NUPRODUCTS program was used to extract data products from the cleaned event lists for both focal plane modules FPMA and FPMB.

The campaign was spread over three observations (60002030002, 60002030004, and 60002030006) comprising 123.9 ks in FPMA and 123.7 ks in FPMB. NGC 1068 is the only well-detected source in the *NuSTAR* FOV and appears unresolved (see Figure 1). As such, spectral products and lightcurves including both the nucleus and the galaxy emission (diffuse + point sources) were extracted using  $75''$  radius apertures (corresponding to  $\approx 81\%$  encircled energy fraction), with backgrounds estimated from blank regions free of contaminating point sources on the same detector (see Figure 1). We find that NGC 1068 is securely detected up to  $\approx 55$  keV at  $3\sigma$  confidence with *NuSTAR*, and has a maximum signal-to-noise of  $\approx 26$  around the peak of Fe  $K\alpha$ .

We also generated a model of the expected background for each FPM within our adopted aperture using NUSKYBGD (Wik et al. 2014). NUSKYBGD uses several user-defined background regions to sample all four detectors in each FPM, which it simultaneously fits in order to model the spectral and angular dependencies for several background components (e.g., instrumental, focused, and unfocused) before ultimately generating the expected background within the adopted aperture. We confirmed the similarity, particularly at high energies where the background makes a significant contribution, between the local and model backgrounds to a few percent. Thus we adopted the local background for simplicity.

Custom position-dependent response matrices and ancillary response files were generated for the spectra of each module, which provide nominal vignetting and point-spread function (PSF) aperture corrections. In total, we have  $\approx 27,300$  and  $\approx 26,100$  counts between 3 and 79 keV in FPMA and FPMB, respectively. As can be seen in Figure 2, the FPMA and FPMB spectra are in excellent agreement, and thus we merged them into a single spectrum using exposure-weighting for convenience, and we use this spectrum for all fitting and plotting purposes (from Figure 3 on). With respect to the *XMM-Newton* EPIC pn instrument, preliminary results suggest *NuSTAR* normalization offsets of  $1.11 \pm 0.01$ ; this value is fully consistent with other *NuSTAR*/*XMM-Newton* cross-calibration

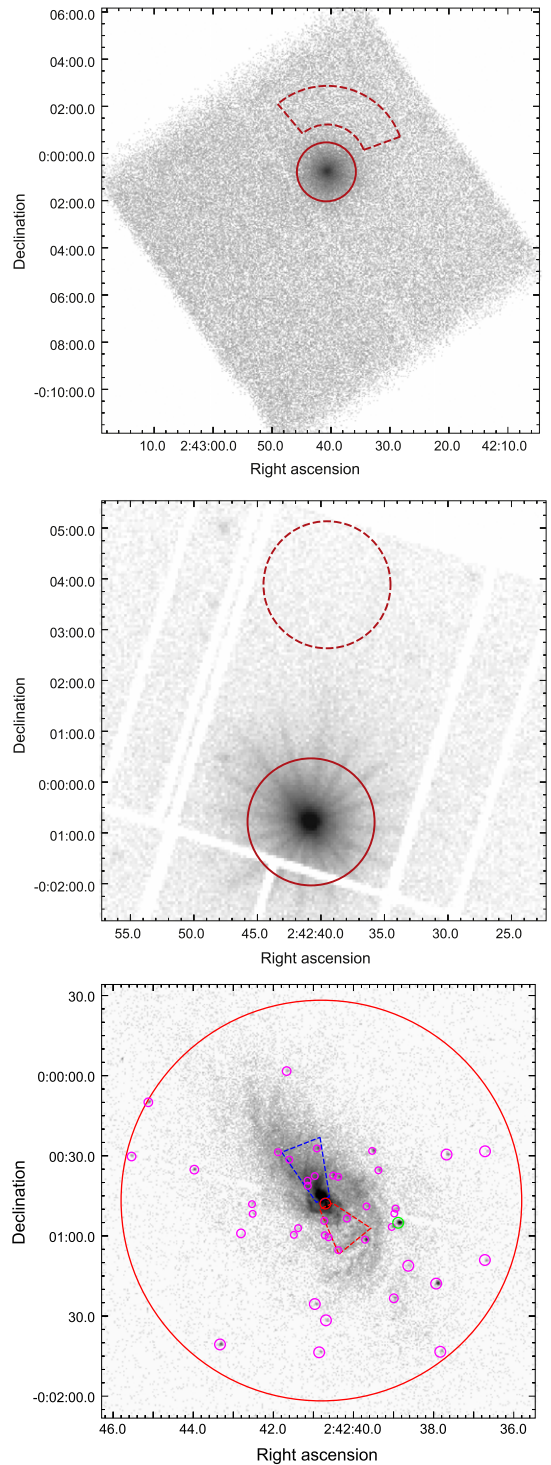


**Figure 1.** (Top) *NuSTAR* 3–79 keV FPMA image of NGC 1068 showing the  $75''$  radius source (solid red circle) and polygon background (dashed red circle) extraction regions. (Middle) *XMM-Newton* 0.2–10 keV pn image of NGC 1068 showing the  $75''$  radius source (solid red circle) and polygon background (dashed red circle) extraction regions. The central point source dominates, although there are hints of faint extended emission. (Bottom) *Chandra* 0.5–8.0 keV ACIS-S image of NGC 1068 showing the  $75''$  aperture used for *NuSTAR* and *XMM-Newton* (large solid red circle). The nucleus is denoted by the small  $2''$  radius (solid red) aperture and is strongly piled up. The obvious off-nuclear point sources (denoted by  $2''$ – $3''$  radius magenta circles) and diffuse emission between  $2''$  and  $75''$  were extracted separately. The rough positions of the radio jet (blue dashed region) and counter jet (red dashed region) are shown (Wilson & Ulvestad 1987). The brightest off-nuclear point source in the *Chandra* image (green circle) was not present after 2000 December 4 and thus has been excluded from analysis. A background was extracted from a source-free region on the same chip, outside this figure.

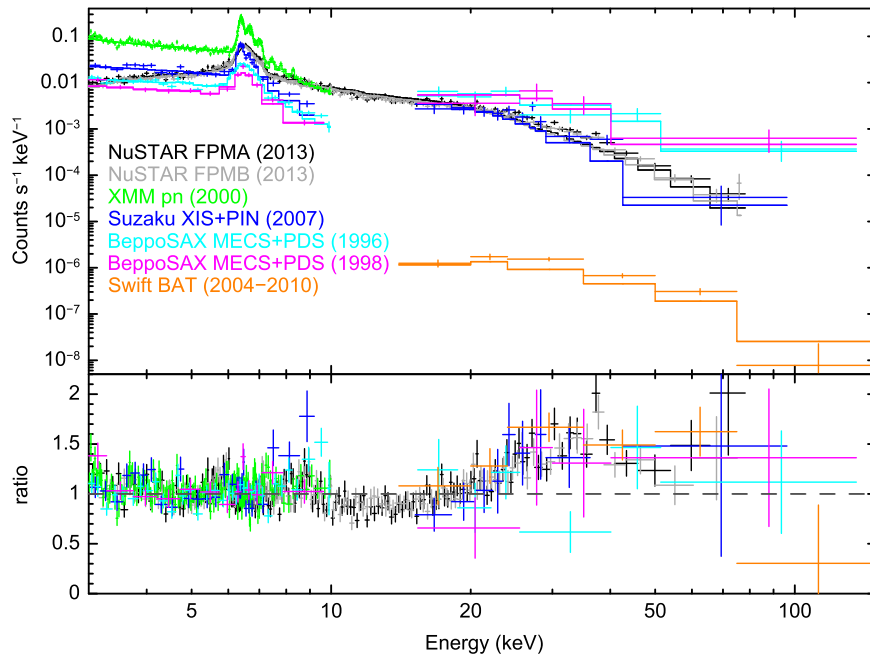


**Figure 2.** Comparison of the *NuSTAR* FPMA/FPMB (black/gray) and *XMM-Newton* pn (green) spectra with other past observations of NGC 1068 from *Suzaku* XIS+PIN (blue), *BeppoSAX* MECS+PDS 1996 (magenta), *BeppoSAX* MECS+PDS 1998 (cyan), and *Swift* BAT (orange), all modeled with the best-fitted two-reflector model M04a. The top panel shows the observed spectra, whereas the bottom panel shows the data-to-model ratios for each spectrum. There is good overall consistency between the various data sets once known normalization offsets are accounted for, with only a few marginally discrepant points seen from the 1996 *BeppoSAX* data. It is clear from the bottom panel that the model provides a poor fit to the data near the Compton reflection hump, with the data peaking at  $\sim 30$  keV, while the `perxray` model peaks at  $\sim 20$  keV. There are some additional residuals around 10–15 keV, indicating that the curvature of the reflection is more severe than the model predicts, as well as around the Fe/Ni line region ( $\approx 6$ –8 keV), suggesting that a few Gaussian lines are insufficient for modeling the complex Fe/Ni emission.

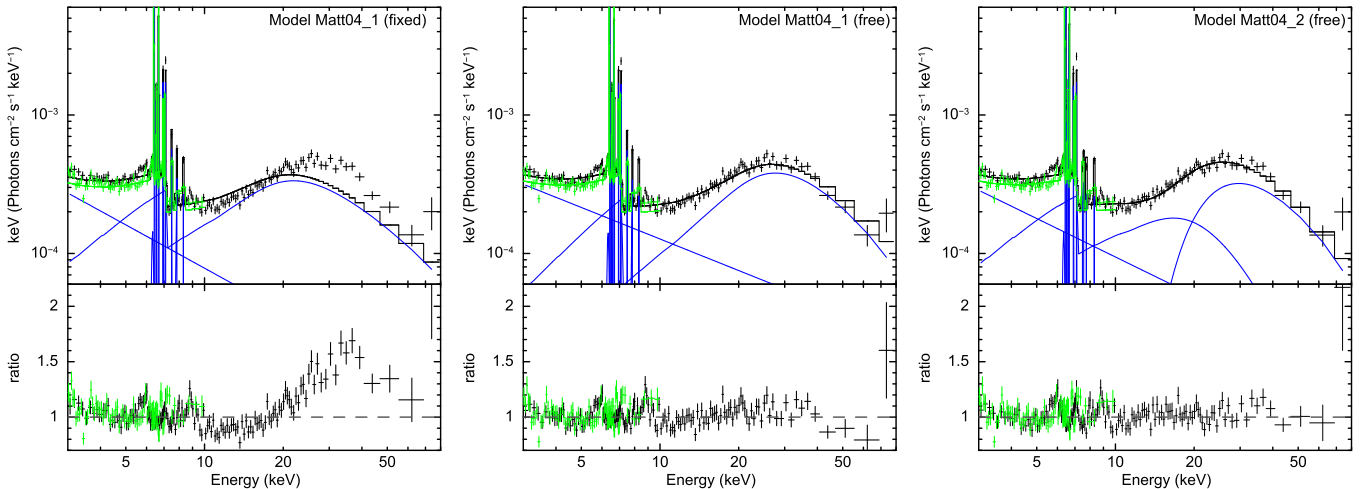


**Figure 3.** Comparison of the *NuSTAR* (black) and *XMM-Newton* pn (green) spectra of NGC 1068, modeled with the best-fitted two-reflector model (blue) where several variables are fixed (*left*; model M04a), fit as free parameters (*middle*; model M04b), and with the addition of a leaky, absorbed transmission component (*right*; model M04c). The top panel shows the observed spectra while the bottom panel shows the data-to-model ratios for each spectrum. The overall fits with the parameters free and the addition of the transmission component (e.g., George et al. 2000) are better, with most of the residuals confined to the complex Fe/Ni line region.

studies (e.g., Walton et al. 2013, 2014). Due to the high signal-to-noise of the *NuSTAR* data, we also find that we need to apply a  $\approx +40$  eV energy offset (i.e.,  $\approx 1$  spectral bin) to bring the intrinsic Fe  $K\alpha$  line energy (6.4007 keV) into agreement with the established redshift of NGC 1068 and the high significance line energy determined by the *Chandra* High Energy Transmission Grating (HETG, Canizares et al. 2000); the reason for the offset is not known, however, its value is within the nominal calibration precision of *NuSTAR* and somewhat smaller offsets have been observed in other sources.

## 2.2. XMM-Newton

NGC 1068 was observed on 2000 July 29–30 with *XMM-Newton* using the EPIC pn and MOS1/MOS2 instruments (Jansen et al. 2001), which provide respective angular resolutions of  $\approx 5''$ – $6''$  FWHM and  $14''$ – $15''$  HPD over the 0.15–12 keV X-ray band. Although the energy resolution of the EPIC detectors (FWHM  $\approx 45$ – $150$  eV between 0.4 and 8 keV) is poorer than *Chandra*'s HETG, the difference narrows to a factor of only  $\approx 5$  by 6–8 keV, and the three EPIC detectors have substantially larger effective areas compared with *Chandra*.

The *XMM-Newton* observation of NGC 1068 was split into two segments made using the Medium filter in Large Window mode (48 ms frame time) for the pn, Full Frame mode (1.4 s frame time) for MOS1, and Small Window mode (0.3 s frame time,  $110'' \times 110''$  FOV) for MOS2. Given the X-ray flux from the AGN, this means that MOS1 will be slightly piled up while MOS2 will not sample the entire  $75''$  radius extraction region (missing some extended emission and requiring a larger PSF correction). To limit systematic uncertainties, we opted to only extract counts for the pn instrument, which comprises 60% of the total *XMM-Newton* collecting area (i.e., MOS1+MOS2 +pn). These are effectively the same conclusions arrived at by Matt et al. (2004, hereafter M04).

We processed both data sets using SAS (v13.0.0) and only single and double events with quality flag = 0. Background flares exceeding 0.3 c/s in the 10–12 keV band of the pn camera were filtered. The remaining good exposures were 32.8 ks for the first observation and 28.7 ks for the second observation, with  $\approx 760,000$  counts between 0.2 and 10.0 keV in total.

Source spectra were extracted from a circular region of  $75''$  radius (corresponding to  $\approx 93.5\%$  encircled energy fraction) centered on the nucleus, to match the *NuSTAR* extraction region. Background photons were selected from a source-free region of equal area on the same chip as the source. We constructed response matrices and ancillary response files using the tasks `RMFGEN` and `ARFGEN` for each observation. Given that the two observations are consecutive and constant within their errors, we merged the spectral products using exposure-weighting. As mentioned previously, we base all of the normalization offsets relative to the *XMM-Newton* pn, which thus has a value of 1.00. Additionally, we find we need to apply a  $\approx +15$  eV energy offset (i.e.,  $\approx 1$  response bin) to bring the intrinsic Fe  $K\alpha$  line energy (6.4007 keV) into agreement with the established redshift of NGC 1068 and the high significance line energy determined by the *Chandra* HETG.

For completeness, we also extracted the Reflection Grating Spectrometer (RGS) data from modules R1 and R2, which provide higher resolution 0.4–2.5 keV spectra for the entire galaxy and can be compared to the *Chandra* HETG data of the nucleus alone. We processed the RGS data using SAS, and removed background flares above 0.1 c/s. Source photons were extracted around the nominal target position with default extraction criteria. Response matrices were created for the first order spectra of R1 and R2 with the task `RGRMFGEN`, which were then combined using the task `RGSCOMBINE`.

### 2.3. *Chandra* HETG and ACIS-S

NGC 1068 was observed many times with *Chandra* with both the ACIS-S detector (Garmire et al. 2003) by itself and the HETG placed in front of the ACIS-S. By itself, ACIS-S has an angular resolution of  $<0.5''$  FWHM and  $\lesssim 0.7''$  HPD, and a spectral resolution of FWHM  $\approx 110$ – $180$  eV between 0.4 and 8 keV. The HETG consists of two different grating assemblies, the High Energy Grating (HEG) and the Medium Energy Grating (MEG), which provide relatively high spectral resolution (HEG: 0.0007–0.154 eV; MEG: 0.0004–0.063 eV) over the entire *Chandra* bandpass (HEG: 0.8–10 keV; MEG: 0.4–8 keV). The gratings operate simultaneously, with the MEG/HEG dispersing a fraction of the incident photons from the two outer/inner High Resolution Mirror Assembly (HRMA) shells, respectively, along dispersion axes offset by

$10^\circ$ , such that they form a narrow X-shaped pattern on the ACIS-S detector. Roughly half of the photons that are not absorbed by the grating pass through undispersed (preferentially the higher-energy photons) and comprise the HETG 0th-order image on ACIS-S with the standard spectral resolution.

We reduced all the *Chandra* data following standard procedures using the CIAO (v4.5) software package and associated calibration files (CALDB v4.5.5.1). The data were reprocessed to apply updated calibrations and energy-dependent sub-pixel event-repositioning (EDSER) techniques, remove pixel randomization, and correct for charge transfer inefficiency (CTI). The data were filtered for standard ASCA grade selection, exclusion of bad columns and pixels, and intervals of excessively high background (none were found). An analysis was performed on reprocessed *Chandra* data, primarily using CIAO, but also with custom software.

The 1st-order HETG spectral products were extracted with standard CIAO tools using an HEG/MEG mask with a full-width of  $4''$  in the cross-dispersion direction centered on the NGC 1068 nucleus; anything smaller than this would suffer from significant energy-dependent PSF losses. The intrinsic ACIS-S energy resolution allows to separate the overlapping orders of the dispersed spectra. The plus and minus sides were combined to yield single HEG and MEG 1st-order spectra. All epochs of the HETG data were combined after double-checking that they did not vary to within errors; obsID 332 appears to have a modestly higher count rate, but this difference is largely below 2 keV and does not materially affect the combined  $>2$  keV spectra. In total, we have 438.7 ks of HETG-resolution nuclear spectra available for spectral fitting (see Table 1 for details), with  $\approx 12,500$  HEG counts between 0.8–10.0 keV and  $\approx 34,000$  MEG counts between 0.4 and 8.0 keV. We consider these to be the least contaminated AGN spectra available below 10 keV (hereafter, simply the HETG “AGN” spectra). The normalization offset between the HEG and MEG was found to be  $1.03 \pm 0.07$ , whereas the offsets with respect to the pn were  $1.05 \pm 0.06$  and  $1.09 \pm 0.06$ , respectively. This is consistent with the cross-calibration findings in Marshall (2012) and Tsujimoto et al. (2011).

In principle, we have a similar amount of HETG 0th-order data, in addition to 47.7 ks of normal ACIS-S data that could be used to model the extranuclear contamination that strongly affects the lower-energy *NuSTAR* and *XMM-Newton* spectra. However, the calibration of the HETG 0th-order still remains somewhat uncertain above  $\sim 5$  keV (M. Nowak 2015, private communication), which we consider critical for extrapolating into the *NuSTAR* band. Thus we chose to model the contamination spectra solely using ACIS-S obsid 344. These data were taken with the nominal 3.2 s frame time, such that the nucleus is heavily piled up ( $\sim 40\%$ ) within  $1''$ – $2''$ . We therefore excluded the inner  $2''$  from the contamination analysis and consider the  $2''$ – $75''$  ACIS-S spectrum to be predominantly emission from the host galaxy (hereafter “host”), although we must consider contributions from the broad wings of the PSF (which only contribute  $\approx 5\%$ – $10\%$  beyond  $2''$  based on PSF simulations) and any truly extended Compton reflection and scattered components from the intrinsic nuclear emission (hereafter “extended AGN”). We replaced readout streak events from the nucleus with an estimate of the background using the `ACISREADCORR` tool.

We note that the brightest off-nuclear point source, CXOU J024238.9–000055.15, which lies  $30''$  to the southwest

of the nucleus in the 344 observation, provides  $\sim 20\%$  of the host contamination counts above 4 keV. Notably, it is not present after 2000 December 4 in either the *Chandra* or *Swift* observations, the latter of which is simultaneous with the *NuSTAR* observation (see Section 2.6). Thus we excluded this point source from our assessment of the host contamination contribution to the *NuSTAR* spectra. The source is present and distinct during the *XMM-Newton* observations, and is found to comprise  $\approx 1.5\%$  of the total  $>4$  keV counts (see also the extended discussion in M04). We account for its presence in the *XMM-Newton* spectrum of NGC 1068 using an additional normalization adjustment between *XMM-Newton* and *NuSTAR*.

To assess host contamination, we extracted ACIS-S spectra of obvious point sources and diffuse emission separately, as shown in Figure 1, using `SPEXTRACT`. For the point sources, we used  $2''$ – $3''$  extraction radii, depending on whether they are strong or weak and whether they reside within strong diffuse emission, while for the diffuse emission we extracted everything else between  $2''$  and  $75''$ . In total, we found  $\approx 6300$  and  $\approx 93450$  0.4–8.0 keV counts for the off-nuclear point source and diffuse components, respectively. A local background region was extracted from an adjacent region  $100''$  in radius  $\approx 3.5'$  northwest of NGC 1068. Ultimately, to simplify the contamination model and improve statistics, we also extracted a total contamination spectrum of all emission within  $2''$ – $75''$ . The normalization offset between the pn and ACIS-S was  $1.04 \pm 0.04$ , which is consistent with the values found by Nevalainen et al. (2010) and Tsujimoto et al. (2011).

#### 2.4. *BeppoSAX*

NGC 1068 was observed by *BeppoSAX* on 1996 December 30 and 1998 January 11 with the Low Energy Concentrator Spectrometer (LECS), the three Medium Energy Concentrator Spectrometers (MECS), and Phoswich Detector System (PDS). We use only the MECS and PDS here.

The MECS contains three identical gas scintillation proportional counters, with an angular resolution of  $\approx 0.7'$  FWHM and  $\approx 2.5'$  HPD, and a spectral resolution of FWHM  $\approx 200$ – $600$  eV between 1.3 and 10 keV. MECS1 failed a few months after launch, so only MECS2 and MECS3 data are available for the 1998 observation. The MECS event files were screened adopting standard pipeline selection parameters. Spectra were extracted from  $3'$  radii apertures and the spectra from individual units were combined after renormalizing to the MECS1 energy-PI relation. Background spectra were obtained using appropriate blank-sky files from the same region as the source extraction. The resulting MECS spectra have  $\approx 5900$  counts between 3 and 10 keV in 100.8 ks of good exposure for the first observation and  $\approx 1550$  counts in 37.3 ks for the second observation. We find that the MECS normalization is systematically offset from the pn by a factor of  $1.12 \pm 0.02$  in the 3–7 keV band and thus by a factor of  $1.02 \pm 0.02$  with respect to *NuSTAR* in the same band.

The PDS has no imaging capability, but does have sensitivity between 15 and 220 keV and provides some constraints above the *NuSTAR* band. The PDS data were calibrated and cleaned using the `SAXDAS` software within `HEASoft`, adopting the “fixed Rise Time threshold” method for background rejection. The PDS lightcurves are known to show spikes on timescales of fractions of second to a few seconds, with most counts from the spikes typically falling below 30 keV. We screened the PDS data for these spikes following

the method suggested in the NFI user guide,<sup>28</sup> arriving at  $\approx 16,600 \pm 3010$  counts between 15 and 220 keV in 62.5 ks of good exposure for the first observation and  $\approx 4720 \pm 1560$  counts in 17.7 ks for the second observation. The PDS spectra were logarithmically rebinned between 15 and 220 keV into 18 channels, although we must cut the spectrum at 140 keV due to poor statistics. With the data quality/binning, it is difficult to appreciate the presence of a bump at 30 keV. The PDS normalization is known to be low by  $\approx 20\%$ – $30\%$  (Grandi et al. 1997; Matt et al. 1997) compared to the MECS, which we accounted for by using a fixed normalization constant of  $0.7 \pm 0.1$  when modeling the data with respect to *NuSTAR*. We note that the statistics for the second *BeppoSAX* observation are poorer, with many of the channels statistically consistent with zero.

#### 2.5. *Suzaku*

The *Suzaku* observatory observed NGC 1068 with the X-ray Imaging Spectrometer (XIS) and Hard X-ray Detector (HXD) PIN instruments on 2007 February 10. Our reduction follows the recommendations of the *Suzaku* Data Reduction Guide.<sup>29</sup>

For the XIS, we generated cleaned event files for each operational detector (XIS0, XIS1, and XIS3) and both editing modes ( $3 \times 3$  and  $5 \times 5$ ) using the *Suzaku* `AEPIPELINE` with the latest calibration, as well as the associated screening criteria files in `HEASoft`. Using `XSELECT`, source spectra were extracted with a  $260''$  radius aperture, while background spectra were extracted from remaining regions free of any obvious contaminating point sources. Responses were generated for each detector using the `XISRESP` script with a medium resolution. The spectra for the front-illuminated detectors XIS0 and XIS3 were consistent, and thus combined using `ADDASCASPEC` to represent the composite XIS spectrum. We obtained  $\approx 33,300$  counts with a good exposure of 61.5 ks. We find that the XIS normalization is systematically offset from the pn by a factor of  $1.17 \pm 0.02$ , which is slightly (i.e.,  $<3\sigma$ ) above the expected normalization offset of  $1.10 \pm 0.01$  assessed by Tsujimoto et al. (2011).

Similar to the PDS, the PIN has poor angular resolution ( $0.56^\circ \times 0.56^\circ$  FOV) but has sensitivity between 15 and 70 keV to compare with *NuSTAR*. We reprocessed the unfiltered event files following the data reduction guide to obtain  $\approx 15,500$  counts with a good exposure of 39.0 ks. No significant detection was found in the GSO. Because the HXD is a collimating instrument, estimating the background requires separate consideration of the non-X-ray instrumental background (NXB) and cosmic X-ray background (CXB), which comprise  $\approx 89\%$  of the total counts. We used the response and NXB files provided by the *Suzaku* team,<sup>30</sup> adopting the model D “tuned” background. Spectral products were generated using the `HXDPINXBPI` tool, which extracts a composite background using the aforementioned NXB and a simulated contribution from the expected CXB following Boldt (1987). We find the PIN normalization to be systematically offset from *NuSTAR* by a factor of  $1.2 \pm 0.05$ , which is consistent with the current cross-calibration uncertainty (Madsen et al. 2015).

<sup>28</sup> <http://heasarc.nasa.gov/docs/sax/abc/saxabc/saxabc.html>

<sup>29</sup> <http://heasarc.gsfc.nasa.gov/docs/suzaku/analysis/>

<sup>30</sup> <http://www.astro.isas.ac.jp/suzaku/analysis/hxd/>

## 2.6. *Swift*

The *Swift* observatory observed NGC 1068 with the X-ray Telescope (XRT; 7" FWHM, 20" HPD) for  $\approx 2$  ks simultaneous with *NuSTAR* on 2012 December 19. The processed data were retrieved from the *Swift* archive, and an analysis was performed using `FTOOLS`. With  $\approx 1200$  counts between 0.5 and 10 keV in a 75" aperture, the *Swift* exposure is not long enough to provide additional constraints beyond those already obtained with *NuSTAR*, *XMM-Newton*, and *Chandra*. However, it does serve to determine if any transient point sources strongly contributed to the  $< 10$  keV *NuSTAR* spectra of NGC 1068. We generated a 0.5–10 keV image with `XSELECT`, which is consistent with the *Chandra* images from 2008 to within the XRT sensitivity and angular resolution limits, and shows no new off-nuclear point sources. The XRT 3–10 keV composite spectrum is also consistent with the other instruments aside from its normalization, which is systematically offset from the pn by a factor of  $1.12 \pm 0.25$ ; the large error bar is due to the fact that the observation only has 64 counts in the 3–10 keV band. This offset is fully consistent with those found by Tsujimoto et al. (2011).

Since 2004 November, the Burst Alert Telescope (BAT) onboard *Swift* (Gehrels et al. 2004) has been monitoring the hard X-ray sky (14–195 keV), providing some constraint above the *NuSTAR* band. *Swift* BAT uses a 5200 cm<sup>2</sup> coded-aperture mask above an array of 32,768 CdZnTe detectors to produce a wide FOV of 1.4 steradian of the sky and an effective resolution of  $\approx 20'$  (FWHM) in stacked mosaicked maps. Based on the lack of variability (see Section 3), we used the stacked 70-month spectrum, which is extracted from the central pixel (2.7; Baumgartner et al. 2013) associated with the BAT counterpart, to assess the nature of the emission. The background-subtracted spectrum contains  $\approx 460$  counts in the 14–195 keV band. We find the BAT normalization to be systematically offset from *NuSTAR* by a factor of  $0.75 \pm 0.05$ , which is consistent with the current cross-calibration uncertainty (Madsen et al. 2015).

## 3. X-RAY VARIABILITY CONSTRAINTS

Depending on the location and structure of the obscuration in NGC 1068, it may be possible to observe temporal variations in one or more of its spectral components on short or long timescales. Notably, there have been previous claims of low-significance variability from the warm reflection component between the *BeppoSAX* and *XMM-Newton* observations (Guainazzi et al. 2000; Matt et al. 2004).

As shown in Table 1, we find reasonable consistency between the count rates extracted from all instruments where NGC 1068 was observed more than once, with differences always less than  $3\sigma$  based on counting statistics. These constraints imply there is no strong continuum variability below 10 keV over periods of 10–15 years. Because *Swift* BAT continuously observes the sky, a new snapshot image can be produced every  $\sim 1$  week for persistent high-energy X-ray sources due to the wide FOV and large sky coverage. To study long-term variability of NGC 1068 (SWIFT\_J0242.6+0000) above 10 keV, we use the publicly available 70-month (9.3 Ms) lightcurves from *Swift* BAT (Baumgartner et al. 2013), which span from 2004 to 2010. The wide energy range of *Swift* BAT allows us to test any underlying energy dependence of the light curve, assessing lightcurves in eight non-overlapping energy

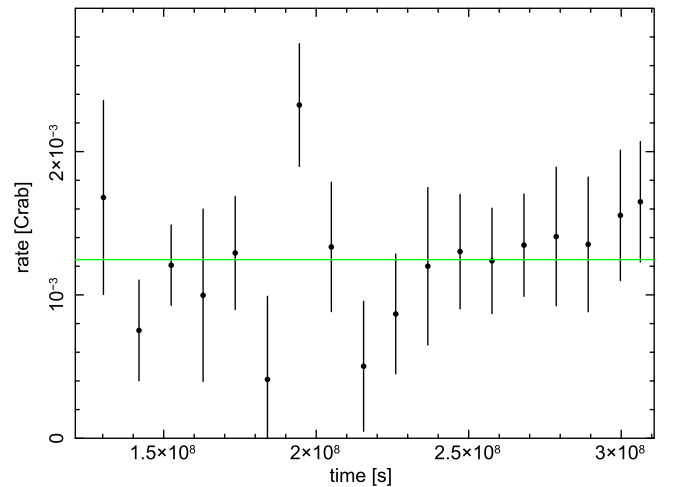


**Figure 4.** *Swift* BAT 70-month 14–195 keV light curve spanning 2004–2010, in bins of  $\approx 0.5$  year. The green line denotes the best-fitted constant model ( $\chi^2_\nu = 0.95$  for  $\nu = 17$ ), indicating that NGC 1068 shows no significant hard X-ray variability over this time span.

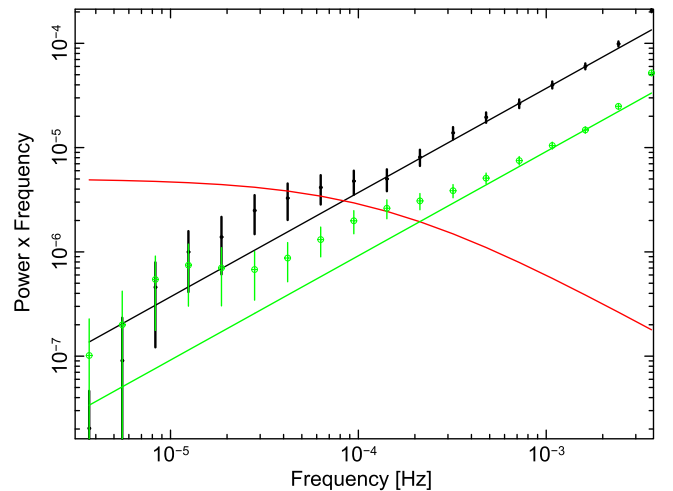


**Figure 5.** Power spectra of the combined 30–79 keV band lightcurves from *NuSTAR* for NGC 1068. The source and background power spectra are plotted in black and green symbols, respectively. The black and green lines denote the power spectra expected for pure Poisson noise for each case. The solid red curve represents the power spectrum of the direct continuum for an AGN of the same mass and accretion rate as NGC 1068. The high-energy lightcurves are roughly consistent (at  $\approx 2\sigma$ ) with simple Poisson noise, although there could be additional low-frequency noise that affects both the source and background variability. Furthermore, backgrounds extracted from the other *NuSTAR* FPM detectors produced similar shapes. Thus we conclude that the variability constraints are significantly below the expected value for a transmitted AGN continuum.

bands: 14–20, 20–24, 24–35, 35–50, 50–75, 75–100, 100–150, and 150–195 keV. The cumulative 14–195 keV light curve, binned in half-year intervals due to the limited statistics, is shown in Figure 4 and is formally constant to within errors ( $\chi^2_\nu = 0.95$  for  $\nu = 17$  degrees of freedom). Variability limits in the individual bands are consistent with the full band results, but are generally less constraining due to limited statistics.

To investigate short-term variability, we applied the Kolmogorov–Smirnov (K–S) test to individual observations, each of which was found to be constant in count rate to  $3\sigma$  confidence. We searched for additional hints of short-term variability using power spectra, taking advantage of the high

throughput of *NuSTAR* above 10 keV. The timescales covered by these light curves ( $\sim 1$ –200 ks) can only probe rapid fluctuations, such as those expected from intrinsic power law emission. Therefore, any variability seen in this range would be indicative of a transmitted power law component (e.g., Markowitz et al. 2003; McHardy et al. 2004, 2005, 2006; Markowitz et al. 2007). Figure 5 shows power spectra from the 30–79 keV band *NuSTAR* lightcurves for NGC 1068 and a typical background region of equal area, which we compare to the expected power spectra for pure Poisson noise and for the expected variability of a pure transmitted component, as observed in unobscured AGN of similar mass and accretion rates. To produce this, we constructed lightcurves in 100 s equally spaced bins, retaining only those that had exposure ratios over 90%. Due to *NuSTAR*'s orbit, *NuSTAR* lightcurves will have 2 ks gaps every 6 ks. Moreover, since *NuSTAR* observed NGC 1068 in three distinct segments, we have larger gaps in between the observations. To mitigate these potential sources of aliasing, we calculated power spectra using the Mexican-hat filtering method described in Arévalo et al. (2012), which is largely unaffected by gaps in the lightcurves. Finally, we normalized the power as the variance divided by the square of the average count rate. As can be seen in Figure 5, the power spectrum detected from NGC 1068 is fully consistent with Poisson noise at better than  $2\sigma$ .<sup>31</sup> Thus, if there is any transmitted component leaking through, it does not comprise the bulk of the  $>10$  keV flux.

We conclude that if there has been any variability from NGC 1068 in the past  $\approx 15$  years, it has been at a level comparable to either the cross-calibration uncertainties between instruments or the statistical uncertainty in the data, and that the short-term behavior as measured by the *NuSTAR* lightcurves is not consistent with a transmitted power law component dominating the flux above 10 keV.

#### 4. X-RAY SPECTRAL CONSTRAINTS

We begin by comparing the high-quality combined *NuSTAR* and *XMM-Newton* spectra with those from several past satellites to demonstrate the dramatic improvement in data quality. We compare all of these with a few common previously used models, which can eventually fit the data relatively well when pushed to extreme values. Following this, we develop a more realistic approach to quantify the non-negligible contamination from extranuclear emission and then model the AGN components using a few common models, such as `pexmon` (Nandra et al. 2007), `MYTorus` (Murphy & Yaqoob 2009; Yaqoob 2012), and `torus` (Brightman & Nandra 2011).

Modeling was performed with `XSPEC` v12.9.0 (Arnaud 1996); quoted uncertainties on spectral parameters are 90% confidence limits for a single parameter of interest and spectral fitting is performed through  $\chi^2$  minimization. Neutral absorption is treated with the `tbabs` absorption code (Wilms et al. 2000), with appropriate solar abundances (`wilm`) and cross sections (`vern`; Verner et al. 1996).

In our analysis, we assume there is no angular dependence of the nuclear emission spectral shape (such that all scatterers see the same photon index) and we neglect any accretion disk

reflection component (e.g., Ross & Fabian 2005; Dauser et al. 2013; García et al. 2014) when modeling the obscured nuclear radiation, which is justified due to the inclination and dominance of scattering and absorption from distant material.

Finally, we note that `XSPEC` has considerable difficulty arriving at the best-fit solution when dealing with large numbers of free parameters, such as we have in NGC 1068 associated with the considerable line emission. Thus, to mitigate this in cases in which we fit individual emission lines separately, we individually fitted the line centers, redshifts, widths, and heights of the Gaussian lines over small portions of the spectrum above a local power law continuum, and then froze each line at its best-fit values. We then fit the relative contributions from the continuum and fluorescent line models.

##### 4.1. Comparison with Previous Models

As mentioned in Section 1, NGC 1068 has been successfully modeled in the past above  $\approx 3$ –4 keV with a double reflector comprising both neutral “cold” (`pexrav` with  $R = -1$ ; Magdziarz & Zdziarski 1995) and ionized “warm” (`cutoffpo`) Compton-scattered components, plus a few Gaussian emission lines to model the strong Fe and Ni emission (hereafter model “M04a,” because it was adopted from M04; see also similar models from Matt et al. 1997; Guainazzi et al. 2000). We therefore began by fitting this model (see Table 2) to the *NuSTAR*, *XMM-Newton*, *BeppoSAX*, *Suzaku*, and *Swift* BAT spectra above 3 keV.

We initially fixed most of the parameters to the values found by M04 (e.g.,  $\Gamma = 2.04$ ,  $Z_{\text{Fe}} = 2.4Z_{\odot, \text{Fe}}$ ,  $\theta_{\text{inc}} = 63^\circ$ ,  $E_{\text{cut}} = 500$  keV),<sup>32</sup> varying only the component normalizations and the redshifts of the emission lines. The normalizations were coupled between the different instruments, while the redshifts differed for each instrument to account for the aforementioned linear energy offsets. The redshifts of the cold reflector and neutral lines ( $K\alpha$ ,  $K\beta$ ) were tied and allowed to vary as one parameter, while the redshifts of the ionized lines were tied and allowed to vary as another parameter. The best fit of model M04a yielded  $\chi^2_\nu = 1.40$  for  $\nu = 1785$  with strong residuals (see Figure 2): The spectral curvature in the continuum around 10–15 keV is poorly modeled, and there is a clear discrepancy between the peak of the reflection hump in the data ( $\sim 30$  keV) and the `pexrav` model ( $\sim 20$  keV); a handful of Gaussians are not sufficient to describe the observed Fe/Ni emission line complexity.

The bottom panel of Figure 2 shows the data-to-model ratios for several past hard X-ray missions compared against the M04a model. After accounting for known cross-calibration offsets, we find that the *NuSTAR*, *XMM-Newton* pn, *Suzaku* XIS, and *BeppoSAX* MECS spectra in the 3–5 keV range, where the warm reflector should dominate, and the 3–10 keV range overall are consistent within their statistical uncertainties based on power law fits to this range. Uncertainties in the normalization offsets between instruments, and hence flux differences, above 10 keV are considerably larger, making it harder to assess potential variability. Nonetheless, after accounting for known cross-calibration offsets, we find that the *NuSTAR*, *Suzaku* PIN, 1998 *BeppoSAX* PDS, and *Swift* BAT spectra above 10 keV are consistent within their statistical uncertainties. The 1996 *BeppoSAX* PDS spectra, however, lack

<sup>31</sup> It is important to stress here that the convolution kernel is broad in frequency, such that nearby power density spectral points will be correlated. Thus the fact that several consecutive points are above the pn level does not make the detection of variability more significant.

<sup>32</sup> Note that in `pexrav`, the inclination angle is specified in units of  $\cos 90 - \theta_{\text{inc}}$ , such that a value of 0.88 is equivalent to  $63^\circ$ .

**Table 2**  
X-ray Spectral Fitting Models

Model	xSPEC Components
Total	
M04a/b	tbabs*(pexrav+cutoffpo+zgauss (Fe <sub>neutral</sub> , Fe <sub>ionized</sub> , Ni <sub>neutral</sub> ))
M04c	tbabs*(MYTZ*cutoffpo+cutoffpo+pexrav+zgauss (Fe <sub>neutral</sub> , Fe <sub>ionized</sub> , Ni <sub>neutral</sub> ))
Nucleus Only	
P	tbabs (tbabs (MYTZ*cutoffpo+C <sub>RRC</sub> +C <sub>RL</sub> +pow+zedge (Ni) *gsmooth (pexmon) +zgauss (Ni Kβ) ) )
M1	tbabs (tbabs (MYTZ*cutoffpo+C <sub>RRC</sub> +C <sub>RL</sub> +pow+highcut*zedge (Ni) *MYTS+gsmooth*MYTL+zgauss (Ni <sub>neutral</sub> )))
M2	tbabs (tbabs (MYTZ*cutoffpo+C <sub>RRC</sub> +C <sub>RL</sub> +pow+highcut*zedge (Ni) *MYTS (0°, 90°) +gsmooth*MYTL (0°, 90°) +zgauss (Ni <sub>neutral</sub> )))
T	tbabs (tbabs (C <sub>RRC</sub> +C <sub>RL</sub> +pow+highcut*gsmooth (torus) ) )
Host Only	
P	tbabs (pcfabs (C <sub>RRC</sub> +C <sub>RL</sub> +pow+zedge (Ni) *gsmooth (pexmon) +zgauss (Ni Kβ) ) )
M1	tbabs (pcfabs (C <sub>RRC</sub> +C <sub>RL</sub> +pow+highcut*zedge (Ni) *MYTS+gsmooth*MYTL+zgauss (Ni <sub>neutral</sub> )))
M2	tbabs (pcfabs (C <sub>RRC</sub> +C <sub>RL</sub> +pow+highcut*zedge (Ni) *MYTS (0°, 90°) +gsmooth*MYTL (0°, 90°) +zgauss (Ni <sub>neutral</sub> )))
T	tbabs (pcfabs (C <sub>RRC</sub> +C <sub>RL</sub> +pow+highcut*gsmooth (torus) ) )

**Note.** We denote Fe<sub>neutral</sub> to signify the modeling of neutral Fe K $\alpha$  (6.40 keV) and K $\beta$  (7.07 keV) transitions, while we use Ni<sub>neutral</sub> for the modeling of neutral Ni K $\alpha$  (7.47 keV) and K $\beta$  (8.23 keV) lines. We denote Fe<sub>ionized</sub> to signify the modeling of ionized Fe K $\alpha$  H-like (6.97 keV), He-like (6.69 keV), and Be-like (6.57 keV) transitions. We denote C<sub>RRC</sub> to signify the modeling of the radiative recombination continuum, which is modeled by a 0.3 keV brems component. We denote C<sub>RL</sub> to signify the modeling of the radiative recombination line emission, which is composed of numerous transitions from a variety of elements. We adopted line species, energies, and strengths consistent with those reported in K14 (which includes Fe<sub>ionized</sub>), as well as Ni He-like K $\alpha$  (7.83 keV). For the ACIS-S host spectrum, we model only a subset of lines comprising just the strongest handful of K14 lines.

the pronounced residuals around 30 keV that are observed in the other hard X-ray spectra, and differ marginally from the rest ( $2.5\sigma$ ). This spectrum alone is relatively well-fitted by the M04a model ( $\chi^2_\nu = 1.43$  for  $\nu = 57$ ), which is perhaps not a surprise because the model is based on these data.

Here, it is important to remember that the *BeppoSAX* PDS, *Suzaku* PIN, and *Swift* BAT spectra are all strongly background-dominated (see Sections 2.4–2.6), and minor variations in background levels (e.g., due to minor flares or how the data are screened) can potentially lead to large variations in the source spectra. The fact that we see an overall consistency in the spectral shape of the residuals, aside from the one discrepant point in the 1996 *BeppoSAX* PDS spectra around 30 keV, demonstrates that no strong variability has been detected over at least the past  $\approx 15$  years.

We note that the  $\chi^2$  residuals are dominated by the *NuSTAR* and *XMM-Newton* pn spectra. Thus, for clarity, we opt to use only the *XMM-Newton* pn and combined FPMA/FPMB *NuSTAR* spectra to represent the global spectrum of NGC 1068 hereafter. To this end, we plot the unfolded *XMM-Newton* pn and composite *NuSTAR* spectra along with the various components that comprise the M04a model in the left panel of Figure 3, as well as the data-to-model residuals. This fit yielded  $\chi^2_\nu = 1.61$  for  $\nu = 1234$ . The continuum parameter values and errors are listed in Table 3, while the normalizations of the various lines are given in Table 4. For *NuSTAR*, the redshifts for the neutral and ionized lines were  $-0.0065^{+0.0005}_{-0.0006}$  and  $0.0081^{+0.0012}_{-0.0010}$ , respectively, whereas for *XMM-Newton* they were  $0.0015^{+0.0003}_{-0.0008}$  and  $0.0026^{+0.0012}_{-0.0013}$ , respectively.

Allowing the power law index, high-energy cutoff, Fe abundance, and inclination angle of the reflector to vary, hereafter model “M04b,” improves the fit substantially to  $\chi^2_\nu = 1.20$  for  $\nu = 1230$ . As shown in Figure 3, most of the residuals are now due to the Fe/Ni line complex, with only very

mild residuals seen from the Compton hump above 10 keV. The emission line parameters remained more or less constant, while the best-fitted values of the other parameters are  $\Gamma = 1.76^{+0.04}_{-0.09}$ ,  $\theta_{\text{inc}} = 70^{+20}_{-7}$ ,  $E_c = 108^{+19}_{-18}$  keV, and  $Z_{\text{Fe}} = 6.8 \pm 0.4$ . The parameter values and errors for model M04b are listed in Table 3.

Another possibility to explain the spectra is for the direct continuum to partially punch through above 20–30 keV; this is often termed the “leaky” torus model, hereafter “M04c.” Given the high column density needed to see direct continuum only above  $\sim 30$  keV, we must properly account for the effects of Compton absorption. For this, we use the multiplicative transmission component from the MYTORUS set of models (hereafter MYTZ to denote “zeroth-order” component; Murphy & Yaqoob 2009) and a cutoff power law (cutoffpl); see also Section 4.2. We tie the values of the intrinsic continuum slope, cutoff energy, and redshift to those of the scattered components, which were left to vary. The normalizations for the three continuum components were free to vary as well. The inclination angle and Fe abundance of the pexrav component of M04c were fixed at  $63^\circ$  and 2.4, respectively, as in M04a, to limit the number of free parameters. This model yielded  $\chi^2_\nu = 1.22$  for  $\nu = 1227$ , with most of the residuals due to the Fe line complex and only very mild residuals around the Compton hump above 10 keV. As before, the emission line parameters remained roughly constant, while the best-fitted values of the other parameters are a photon index of  $\Gamma = 1.92^{+0.05}_{-0.06}$ , an exponential cutoff rollover energy of  $E_c = 22^{+24}_{-9}$  keV, a column density for the absorbed transmission component of  $N_{\text{H}} > 9.95 \times 10^{24} \text{ cm}^{-2}$ , and normalizations of  $A_{\text{trans}} = 67.8^{+2.5}_{-1.8}$ ,  $A_{\text{warm}} = (7.9^{+0.5}_{-0.5}) \times 10^{-4}$ , and  $A_{\text{cold}} = (1.1^{+2.5}_{-1.8}) \times 10^{-2}$  (all in units of photons  $\text{keV}^{-1} \text{ cm}^{-2} \text{ s}^{-1}$  at 1 keV). Parameter values for model M04c are listed in Table 3.

Clearly, model M04a provides a poor fit to the *NuSTAR* data, while both of the alternative models, M04b and M04c appear to

**Table 3**  
Model Spectral Fit Parameters

(1)	(2)	(3)	(4)	(5)	(6)	(7)	(8)	(9)	(10)	(11)	(12)	(13)
Model	Spectra	Range	$\Gamma$	$N_{\text{H}}$	$E_c$	$\theta_{\text{inc}}$	$\theta_{\text{open}}$	$Z_{\text{Fe}}$	S/L ratio	$\log F_{\text{X, cold}}$	$\log F_{\text{X, warm}}$	$\chi^2_{\nu}$ ( $\nu$ )
Total (Previous Models)												
M04a	XN	3–79	2.04	10	500	63	...	2.4*	...	$-11.70^{+0.01}_{-0.01}$	$-11.67^{+0.01}_{-0.01}$	1.61 (1234)
M04b	XN	3–79	$1.76^{+0.04}_{-0.09}$	10	$108^{+19}_{-18}$	$70_{-7}$	...	$6.8^{+0.4*}_{-0.4}$	...	$-11.86^{+0.02}_{-0.02}$	$-11.57^{+0.01}_{-0.01}$	1.20 (1230)
M04c	XN	3–79	$1.92^{+0.05}_{-0.06}$	$10_{-0.05}$	$22^{+24}_{-9}$	63	...	2.4*	...	$-11.74^{+0.01}_{-0.01}$	$-11.64^{+0.01}_{-0.01}$	1.22 (1227)
Nucleus Only												
P	H	0.5–9	$2.46^{+0.02}_{-0.24}$	10	500	85	...	$4.5^{+1.1}_{-0.6}$	...	$-11.80^{+0.02}_{-0.02}$	$-11.75^{+0.04}_{-0.04}$	1.60 (1472)
P	H	2–9	$1.15^{+0.32}_{-0.08}$	10	500	85	...	$5.1^{+3.7}_{-0.9}$	...	$-11.77^{+0.12}_{-0.17}$	$-11.79^{+0.14}_{-0.22}$	0.66 (319)
M1	H	0.5–9	$1.40^{+0.12}_{-0.08}$	10	500	90	60	...	$0.42^{+0.12}_{-0.08}$	$-11.82^{+0.08}_{-0.05}$	$-11.81^{+0.02}_{-0.02}$	1.64 (1472)
M1	H	2–9	$1.40^{+0.16}_{-0.08}$	10	500	90	60	...	$0.46^{+0.12}_{-0.08}$	$-11.73^{+0.02}_{-0.07}$	$-11.87^{+0.10}_{-0.09}$	0.72 (319)
M2	H	0.5–9	$2.60^{+0.02}_{-0.19}$	10	500	0.90	60	...	$0.67^{+0.09}_{-0.09}$	$-11.54^{+0.02}_{-0.02}$	$-12.36^{+0.14}_{-0.16}$	1.62 (1471)
M2	H	2–9	$1.52^{+0.01}_{-0.08}$	10	500	0.90	60	...	$0.64^{+0.13}_{-0.11}$	$-11.87^{+0.14}_{-0.11}$	$-11.76^{+0.03}_{-0.03}$	0.74 (318)
T	H	0.5–9	$1.30^{+0.09}_{-0.05}$	10	...	87	$67^{+12}_{-15}$	...	...	$-11.78^{+0.03}_{-0.05}$	$-11.76^{+0.02}_{-0.02}$	1.65 (1472)
T	H	2–9	$1.14^{+0.33}_{-0.08}$	10	...	87	$67^{+11}_{-17}$	...	...	$-11.82^{+0.30}_{-0.09}$	$-11.69^{+0.06}_{-0.09}$	0.73 (319)
Host Only												
P	A	0.5–9	$2.49^{+0.02}_{-0.19}$	...	500	85	...	$33^{+40}_{-13}$	...	$-12.47^{+0.08}_{-0.15}$	$-12.09^{+0.04}_{-0.01}$	1.42 (163)
P	A	2–9	$2.49^{+0.02}_{-0.40}$	...	500	85	...	$100^{+3.7}_{-60}$	...	$-12.45^{+0.11}_{-0.22}$	$-12.11^{+0.09}_{-0.03}$	0.81 (73)
M1	A	0.5–9	$2.55^{+0.06}_{-0.06}$	10	500	90	60	...	$2.46^{+3.49}_{-1.01}$	$-12.37^{+0.11}_{-0.16}$	$-12.11^{+0.03}_{-0.03}$	1.44 (163)
M1	A	2–9	$2.60^{+0.02}_{-0.42}$	10	500	90	60	...	$2.27^{+0.07}_{-0.90}$	$-12.35^{+0.07}_{-0.38}$	$-12.12^{+0.10}_{-0.03}$	0.89 (73)
M2	A	0.5–9	$2.56^{+0.06}_{-0.06}$	10	500	0.90	60	...	$2.25^{+0.65}_{-0.90}$	$-12.36^{+0.10}_{-0.15}$	$-12.11^{+0.04}_{-0.03}$	1.44 (162)
M2	A	2–9	$2.60^{+0.02}_{-0.35}$	10	500	0.90	60	...	$2.70^{+5.20}_{-1.09}$	$-12.34^{+0.10}_{-0.33}$	$-12.13^{+0.10}_{-0.03}$	0.87(72)
T	A	0.5–9	$2.61^{+0.06}_{-0.06}$	10	...	87	$26^{+13}_{-26}$	...	...	$-12.24^{+0.07}_{-0.08}$	$-12.17^{+0.03}_{-0.03}$	1.49 (163)
T	A	2–9	$2.91^{+0.07}_{-0.39}$	10	...	87	$26^{+17}_{-26}$	...	...	$-12.17^{+0.10}_{-0.10}$	$-12.25^{+0.10}_{-0.17}$	0.94 (73)
Total (Previous Models)												
Pa	HAXNB	2–195	$1.57^{+0.02}_{-0.02}$	10	500	85	...	$5.0^{+0.3}_{-0.3}$	...	$-11.87^{+0.02}_{-0.02}$	$-11.90^{+0.02}_{-0.02}$	1.34 (1666)
M1a	HAXNB	2–195	$1.40^{+0.09}_{-0.01}$	10	500	90	...	...	1	$-14.00^{+0.30}_{-0.30}$	$-11.67^{+0.01}_{-0.01}$	3.78 (1666)
M1d	HAXNB	2–195	$1.40^{+0.12}_{-0.12}$	$9.4_{-3.3}$	$41^{+5}_{-4}$	$78^{+3}_{-4}$	...	...	$3.8^{+0.5}_{-0.8}$	$-12.44^{+0.04}_{-0.04}$	$-11.78^{+0.01}_{-0.01}$	1.31 (1662)
M1g	HAXNB	2–195	$1.40^{+0.34}_{-0.01}$	10	$34^{+58}_{-4}$	$80.7^{+6.5}_{-3.4}$	...	...	$3.3^{+0.8}_{-0.5}$	$-12.05^{+0.01}_{-0.01}$	$-11.97^{+0.02}_{-0.02}$	1.29 (1660)
M2a	HAXNB	2–195	$2.29^{+0.04}_{-0.02}$	10	500	90	...	...	1	$-11.87^{+0.01}_{-0.02}$	$-12.83^{+0.17}_{-0.29}$	1.83 (1666)
M2d	HAXNB	2–195	$2.10^{+0.06}_{-0.07}$	$10.0_{-0.3}$	$128^{+115}_{-44}$	90	...	...	$1.0^{+0.1}_{-0.1}$	$-11.81^{+0.02}_{-0.02}$	$-12.34^{+0.05}_{-0.05}$	1.14 (1666)
Ta	HAXNB	2–195	$1.96^{+0.05}_{-0.04}$	10	500	87	$64^{+3}_{-2}$	1	...	$-11.95^{+0.02}_{-0.03}$	$-11.86^{+0.02}_{-0.02}$	1.61 (1667)
Tc	HAXNB	2–195	$2.13^{+0.04}_{-0.06}$	$6.3^{+0.6}_{-0.8}$	500	$87_{-12}$	$69^{+4}_{-3}$	1	...	$-11.96^{+0.02}_{-0.03}$	$-11.87^{+0.02}_{-0.02}$	1.57 (1663)

**Note.** *Column 1:* model used. Model name beginning with “M04” denote variations of M04 models, “P” denote variations of pexmon models, “M1” denote variations of coupled MYTORUS models, “M2” denote variations of decoupled MYTORUS models, and “T” denote variations of TORUS models. See Sections 4.1 and 4.2 for details. When multiple rows are listed, the first one or two rows represent the nucleus model while the second or third row represents the host model. *Column 2:* spectra fit, where X = XMM-Newton pn, A = Chandra ACIS-S, H = Chandra HEG+MEG, N = NuSTAR, and B = Swift BAT. *Column 3:* energy range fit, in keV. *Column 4:* photon index of the primary transmitted power law continuum. Note that some reported limits are poorly constrained since the allowed ranges for  $\Gamma$  are confined to between 1.1 and 2.5 for the pexmon model, between 1.4 and 2.6 for the MYTORUS model, and between 1 and 3 for the TORUS model. *Column 5:* neutral hydrogen column density of the obscuring torus/clouds, in units of  $10^{24} \text{ cm}^{-2}$ . *Column 6:* energy of the exponential cutoff rollover of primary transmitted power law continuum, in keV. *Column 7:* inclination angle with respect to a face-on geometry, in degrees. Note that some reported limits are poorly constrained because the allowed ranges for  $\theta_{\text{inc}}$  are confined to  $0^\circ$ – $72^\circ$  for the M04 (pexrav) model,  $0^\circ$ – $85^\circ$  for the pexmon model, and  $18^\circ$ – $87^\circ$  for the TORUS model. *Column 8:* Torus opening angle, in degrees. This parameter is not meaningful for the M04 and pexmon models, is fixed at  $60^\circ$  for the MYTORUS model, and is confined to  $25^\circ$ – $84^\circ$  for the TORUS model. *Column 9:* Fe abundance with respect to our adopted value of  $Z_{\odot, \text{Fe}}$ . The overall abundance of metals (not including Fe) is assumed to be solar ( $Z_{\odot}$ ). Note that entries denoted by \* are for pexrav, where the Fe abundance is driving the peak of the Compton reflection hump to higher energy and has no effect on the Fe line emission, which is modeled with Gaussians. *Column 10:* ratio of the scattered and line components of MYTORUS. This can crudely be interpreted as an Fe abundance with respect our adopted value of  $Z_{\odot, \text{Fe}}$ , although care should be taken because the correspondence is non-trivial and hence only approximate (Yaqoob 2012). *Columns 11–12:* logarithms of the 2–10 keV fluxes of the cold and warm reflection components, respectively, in units of  $\text{erg s}^{-1} \text{ cm}^{-2}$ . *Column 13:*  $\chi^2_{\nu}$  and degrees of freedom for a given model. Values with no quoted errors were fixed at their specified values.

**Table 4**  
Fe and Ni Line Fluxes (with Model M04b)

Line	<i>XMM-Newton</i>		<i>Chandra</i>	
	M04 <40''	This Work <75''	HETG <2''	ACIS-S 2''–75''
Fe neutral K $\alpha$	44.3	47.4 <sup>+1.9</sup> <sub>-2.2</sub>	38.9 <sup>+3.8</sup> <sub>-3.8</sub>	17.5 <sup>+3.3</sup> <sub>-3.3</sub>
Fe neutral K $\alpha$ CS	8.7	3.8 <sup>+1.5</sup> <sub>-2.2</sub>	4.2 <sup>+3.6</sup> <sub>-2.2</sub>	<1.5
Fe neutral K $\beta$	9.1	8.9 <sup>+1.1</sup> <sub>-1.5</sub>	4.3 <sup>+3.1</sup> <sub>-1.9</sub>	<5.2
Ni neutral K $\alpha$	5.6	5.8 <sup>+1.8</sup> <sub>-0.9</sub>	<7.3	<8.8
Ni neutral K $\beta$	3.2	3.1 <sup>+0.9</sup> <sub>-1.3</sub>	<19.8	<16.8
Fe Be-like 6.57 keV	7.6*	8.0 <sup>+1.5</sup> <sub>-2.1</sub>	6.3 <sup>+2.1</sup> <sub>-2.5</sub>	3.9 <sup>+2.9</sup> <sub>-2.9</sub>
Fe He-like 6.69 keV	22.8*	27.8 <sup>+1.0</sup> <sub>-2.9</sub>	12.8 <sup>+3.9</sup> <sub>-2.3</sub>	6.1 <sup>+2.4</sup> <sub>-2.4</sub>
Fe H-like 6.97 keV	7.1*	8.2 <sup>+0.8</sup> <sub>-2.5</sub>	7.7 <sup>+1.5</sup> <sub>-3.8</sub>	<6.1
Ni He-like 7.83 keV	2.7*	3.9 <sup>+1.1</sup> <sub>-1.1</sub>	<10.2	<10.4

**Note.** *Column 1*: primary Fe and Ni lines measured in M04 and here using the *XMM-Newton* and *Chandra* data sets. The continuum was fit in all cases with the M04b model for consistency. *Columns 2–5*: normalizations of the best-fitted *zgauss* components to each line, in units of  $10^{-6}$  photons  $s^{-1} cm^{-2}$ . The components denoted by \* were mistakenly listed in Table 3 of M04 with values a factor of 10 higher than intended (G. Matt 2015, private communication); they have been corrected here for clarity. The difference between *XMM-Newton* pn values is at least partially due to differences in encircled energy fractions (87% vs. 93%) between the extraction regions.

yield more reasonable fits. The Fe abundance from M04b is substantially supersolar, which is consistent with past constraints on NGC 1068 (e.g., K15; Kraemer et al. 1998; Kinkhabwala et al. 2002), as well as some unobscured AGN (e.g., Fabian et al. 2009, 2013; Parker et al. 2014), although such results are not necessarily definitive. The overabundance is at least partially driven by the need to fit the 30 keV bump with a much deeper iron edge. Model M04c provides an equally acceptable fit, although it requires that the transmitted component dominates above 20 keV with rather unusual best-fit parameters. For instance, the cutoff energy implies a unrealistically low corona temperature (e.g., Petrucci et al. 2001), while the ratio of transmitted-to-scattered normalizations is abnormally high ( $\approx 6000$ ). As such, this scenario seems unlikely on its own and can be further ruled out by the variability constraints presented in Sections 2.1 and 2.6, which imply that NGC 1068 has been more or less constant over all the timescales that we have measured.

While the simple models described above appear to fit the global *NuSTAR* and *XMM-Newton* spectra to reasonably acceptable levels, we caution that such fits can be deceptive and misrepresent underlying complex structure. As shown in the following sections, including higher spectral and angular resolution data from *Chandra* allows us to remove potential host contamination and probe the nature of the complex scattering medium in more detail. Additionally, a critical drawback of the *pexrav* model is that it models a simple slab-like geometry for the Compton scatterer assuming an infinite column density, which is known to incorrectly describe the true physical situation (e.g., a smooth or clumpy torus with finite column thickness) present in NGC 1068. To this end, we also explore a few models that adopt more realistic geometrical scenarios for AGN scattering in Section 4.2.

#### 4.2. Detailed Spectral Modeling

At this point, it is critical to define which spectral models we will fit to the data, because there are a variety of models of

Compton-scattered emission that have been used to fit reflection-dominated spectrum to account for the possible different geometries of the scattering material. These include:

1. *pexmon*—this is a modified version of the standard *pexrav* model (Magdziarz & Zdziarski 1995), already used in Section 4.1, self-consistently computes the continuum (based on *pexrav*) as well as the neutral Fe K $\alpha$ , Fe K $\beta$ , and Ni K $\alpha$  emission lines (based on Monte Carlo simulations by George & Fabian 1991), as well as the Fe K $\alpha$  Compton shoulder (Nandra et al. 2007). As with *pexrav*, this model assumes that the scattering structure has a slab geometry and infinite optical depth. Moreover, the total and Fe abundances can be adjusted to account for non-solar values. The Ni edge is not included in this model, so we add this as a *zedge* component at the systemic redshift, the depth of which is tied to the the measured Ni K $\alpha$  flux (a value of  $\tau = 0.1$  in *zedge* achieved this). Results for the series of *pexmon* Compton scattering models are detailed below and summarized in Table 3. We caution that the *pexmon* model is limited to photon indices between  $\Gamma = 1.1$ –2.5 and inclination angles  $\theta = 0^\circ$ –85°.
2. *MYTORUS*—functions for a smoothly distributed toroidal reprocessor composed of gas and dust with finite optical depth and a fixed 60° opening angle (Murphy & Yaqoob 2009); we do not consider this to be a severe limitation, because other X-ray models and NLR and MIR modeling imply a  $\sim 60^\circ$  opening angle for NGC 1068. *MYTORUS* is composed of three separate spectral components: a transmitted intrinsic continuum component (*MYTZ*, incorporated as a multiplicative table), which represents the photons along the direct line of sight to the nucleus that remain after scattering, as well as Compton-scattered continuum (hereafter *MYTS*) and fluorescent line and Compton shoulder (hereafter *MYTL*) components, which represent photons scattered into our line of sight from a different viewing angle to the nucleus (both additive table models). The neutral Fe lines are modeled self-consistently with the Compton-scattered component. By using multiple scatterers, varying their relative normalizations and/or inclination angles with respect to our line of sight, disentangling their column densities, and so forth, Yaqoob (2012) demonstrated that one could model a wide range of possible geometries surrounding the central engine. The Ni edge is not included in this model, so we add it as a *zedge* component at the systemic redshift, the depth of which is tied to the measured Ni K $\alpha$  flux (which empirically equates to fixing  $\tau = 0.1$ ). The model does not allow dynamic fitting for a high-energy cutoff, and table models are only computed for a handful of fiducial “termination” energies ( $E_T$ , which is effectively an instant cutoff).<sup>33</sup> For expediency, we chose to implement a dynamic cutoff separately using

<sup>33</sup> Below energies of  $\approx 20$  keV, the *MYTORUS* models with different termination energies are virtually identical, whereas above this value the lower termination energy models have pseudo-exponential cutoffs, the forms of which depend modestly on input parameters. Using a sharp termination compared with an exponential cutoff should lead to mild differences in the shape of the cutoff. Unfortunately, the lack of any continuum above the termination energy imposes parameter limitations when fitting, for example, the *Swift* BAT spectrum. While there may be merits to the arguments given in the *MYTORUS* manual against applying a cutoff, we find the alternative, a dramatic cutoff, to also be unsatisfactory from a physical standpoint.

the  $E_T = 500$  keV model multiplied by the `highcut` model with a fixed pivot energy of 10 keV and an e-folding energy that is tied to the transmitted power law cutoff energy.<sup>34</sup> It is argued in the `MYTorus` manual that applying a high-energy cutoff ruins the self-consistency of the `MYTorus`; therefore, once we determined an approximate  $E_{\text{cut}}$  for our best-fit model, we dropped the use of `highcut` and replaced the  $E_T = 500$  keV model with one that best approximates  $E_{\text{cut}} = E_T$ . Results for the series of `MYTorus` Compton scattering models are detailed below and summarized in Table 3. We caution that the `MYTorus` model is computed only for photon indices between  $\Gamma = 1.4$ –2.6, to energies between 0.5 and 500 keV, and solar abundances.

3. `torus`—this model describes obscuration by a spherical medium with variable  $N_{\text{H}}$  and inclination angle, as well as a variable biconical polar opening angle (Brightman & Nandra 2011). `Torus` self-consistently predicts the  $K\alpha$  and  $K\beta$  fluorescent emission lines and absorption edges of all the relevant elements. The key advantage of this model is it can fit a range of opening angles and extends up to  $N_{\text{H}} = 10^{26}$  cm<sup>2</sup>, but a major drawback is that it does not allow the user to separate the transmitted and Compton-scattered components. As such, it can only be applied to the nuclear emission and is not appropriate to model the host component, which should include only the Compton-scattered emission. As with `MYTorus`, `torus` does not allow dynamic fitting for a high-energy cutoff, so we implemented a cutoff using `highcut` in the same manner as for `MYTorus`. Results for the series of `torus` Compton scattering models are detailed below and summarized in Table 3. We caution that the `torus` model is limited to photon indices between  $\Gamma = 1.0$ –3.0, inclination angles  $\theta_{\text{inc}} = 18^\circ$ –87°, opening angles  $\theta_{\text{tor}} = 25^\circ$ –84°, and solar abundances.

Both `MYTorus` and `torus` provide significant and distinct improvements over the geometric slab model that manifest in the spectral shapes of both line and continua. Nonetheless, note that they only sample a small portion of the potential parameter space that likely describes real gas distributions in the vicinity of AGN. As in Section 4.1, we model the transmitted power law continuum as `MYTZ*cuttoffpl` where applicable.

Before we proceed to fitting these more complex models, we note that while *NuSTAR* and *XMM-Newton* have large collecting areas and wide energy coverage, neither is able to spatially separate the spectra of the AGN from various sources of host contamination (or even extended AGN emission from point-like AGN emission), nor are they able to spectrally resolve some line complexes to gain a better understanding of the physical processes involved (e.g., K14; Kinkhabwala et al. 2002). We rely on *Chandra* data for these purposes, allowing us to construct the most robust model to date for the nuclear and global spectra of NGC 1068. We use *Chandra* HETG spectra to model the point-like nuclear emission from NGC 1068 from the inner 2'' in Section 4.2.1 and use the

<sup>34</sup> While applying exponential cutoffs outside `MYTorus` is expressly warned against in the `MYTorus` manual, we found that this method yielded reasonable consistency compared with the various `MYTorus` termination energy models over the ranges of parameters we fit, such that constraints on the cutoff energies typically were less than a factor of two different from the termination energy considered.

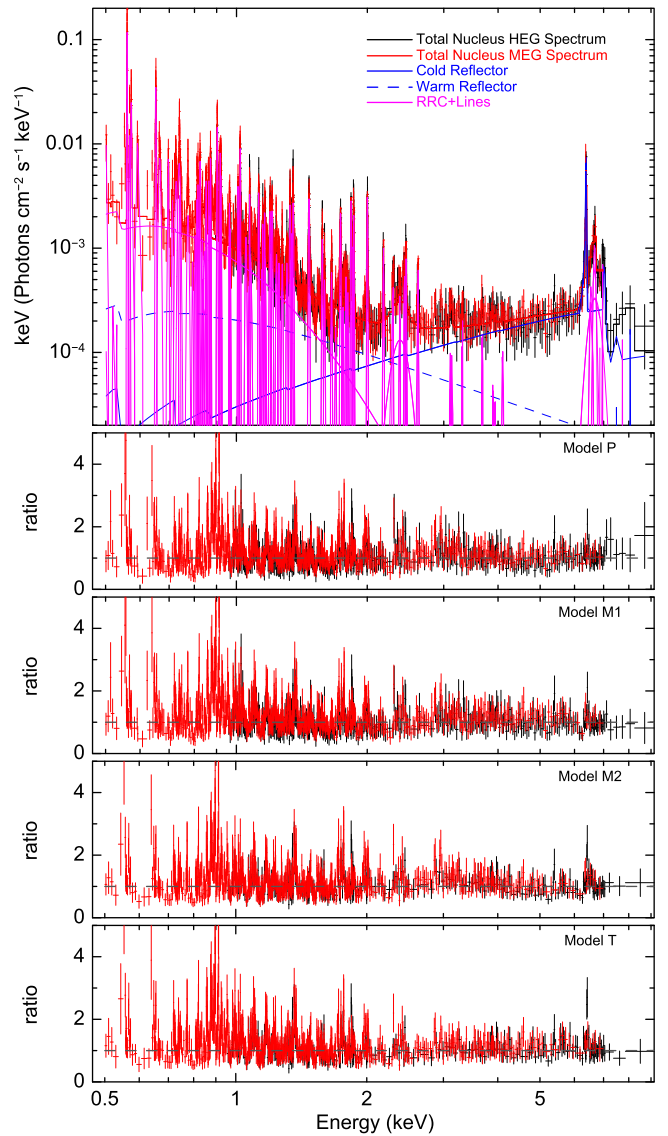


**Figure 6.** HEG (black) and MEG (red) unfolded spectra of nucleus of NGC 1068 extracted from a 4'' full-width mask. The spectra are fitted with four models composed of partially absorbed cold and warm reflectors (blue solid and dashed lines, respectively), as well as RRC and line components as identified by K14 (magenta solid lines). The top panel shows the fit to model P while the rest of the panels show the data-to-model ratios for models P, M1, M2, and T, respectively.

*Chandra* ACIS-S data to model the host galaxy emission from NGC 1068 between 2 and 75'' in Section 4.2.2, both of which are fit between 0.5 and 9.0 keV. Fitting down to 0.5 keV allows us to constrain the soft-energy components, which can affect the flux and slope of the ionized reflector if unaccounted for. We then proceed to fit the combination of the nuclear and host galaxy emission to the *NuSTAR*, *XMM-Newton*, and *Chandra* spectra in Section 4.2.4. We also fit the *Swift* BAT spectra with this combined spectrum, because the BAT spectrum provides some additional spectral coverage up to  $\approx 200$  keV and its spectral shape more or less agrees with *NuSTAR* where the two spectra overlap (see Figure 2).

#### 4.2.1. Point-like Nuclear Emission

The HETG nuclear spectra are shown in Figure 6, and clearly exhibit emission from several different components. To

reproduce the main features of the HETG spectra, we assume that the nucleus AGN spectrum has a direct transmitted power law (`cutoffpl`) with slope  $\Gamma_{\text{nuc}}$  and cutoff energy  $E_{\text{c,nuc}}$ , which is absorbed by a presumably Compton-thick absorber (e.g., an edge-on torus) with neutral column density  $N_{\text{H}}$  (modeled as `MYTZ*cutoffpl`). Based on the modeling in Section 4.1, we adopt fixed values of  $N_{\text{H}} = 10^{25} \text{ cm}^{-2}$  and  $\theta_{\text{inc}} = 90^\circ$  for the absorber; these quantities are poorly constrained by the  $<10 \text{ keV}$  data alone, due to degeneracies with other spectral components (see below). Although the transmitted component is not observable below  $\sim 10 \text{ keV}$  (if at all) in Compton-thick AGN, most of the observed  $<10 \text{ keV}$  features should be indirect products of it.

We empirically model the soft RRC and RL emission as a bremsstrahlung component (`bremss`, best fit  $kT_{\text{bremss}} = 0.31 \pm 0.03 \text{ keV}$  and  $A_{\text{bremss}} = 0.013 \pm 0.01 \text{ cm}^{-2}$ ) and  $\approx 90$  narrow ionized emission lines (`zgauss`), respectively. The latter are based on the line identifications from K14 plus Ni He-like 7.83 keV. For simplicity, we adopt a single redshift  $z_{\text{ion}}$  and line width  $\sigma_{\text{ion}}$  (fixed at 0.0035 keV) for the vast majority of the ionized lines. The line normalizations are in crude agreement with K14, although there are differences due to our adopted widths and redshifts; as these are primarily used so that we can constrain the RRC `bremss` temperature and normalization, we do not report the line properties here. Even with all of these components, significant complex Fe and Si line emission remains (see Figure 6; residuals can also be seen in Figures 1–4 of K14), which we modeled empirically as a broad  $\sigma = 0.2 \text{ keV}$  line centered at 6.69 keV and a broad  $\sigma = 0.1 \text{ keV}$  line centered at 2.38 keV, respectively, which reduced the residuals significantly.

The hard X-ray emission is modeled with a “warm” scattered power law reflector and “cold” Compton-scattered continuum plus emission lines. For the former component, we naively adopt a power law with the same intrinsic slope as the obscured transmitted component.<sup>35</sup> For the latter component, we adopt either `pexmon`, `MYTorus`, or `torus`, as described above, none of which is particularly well-constrained by the *Chandra* HETG data alone. The cold reflection models were all smoothed with an 0.01 keV Gaussian to best-match the HETG neutral Fe  $K\alpha$  line width. We added neutral Ni  $K\alpha$  (7.47 keV) and/or  $K\beta$  (8.23 keV) lines when these were not modeled explicitly by the cold reflection models; these lines are poorly constrained by the HETG spectra, and thus were fixed relative to the full extraction region values from *XMM-Newton* assuming a nuclear to galaxy ratio of 2:1, as found for neutral Fe  $K\alpha$  (see Section 4.2.3). Similar to the transmitted component, we fixed the reflection component inclination angle to  $\theta_{\text{inc}} = 90^\circ$ , which is close to the nominal viewing angle associated with NGC 1068, and the high-energy exponential cutoff rollover energy to  $E_c = 500 \text{ keV}$  for all models. Finally, we included two neutral absorption (`tbabs`) components, one of which was fixed at the Galactic column while the other was

<sup>35</sup> The warm mirror gas in NGC 1068 is possibly the same warm absorber gas seen in many Seyfert 1s (e.g., K14), in which case the ionization level of the gas is not sufficiently high to be a perfect mirror. As noted in Section 1, this could imprint significant absorption edges/lines on the spectrum up to several keV (e.g., Kaspi et al. 2002), effectively adding spectral curvature, primarily below 2 keV, or flattening the slope of this component. We tested the possible effects of this modification on our results using an ionized absorber produced by `XSTAR` for NGC 3227 (see Markowitz et al. 2009, for details). The primary effect was an increase in the normalization of the RRC component, with little change to the parameters of the components that dominate above 2 keV. Given this outcome, we chose a perfect mirror for simplicity.

fit as  $N_{\text{H}} = (1.5^{+0.2}_{-0.1}) \times 10^{21} \text{ cm}^{-2}$  to constrain the host column density in NGC 1068.

We now proceed to fit the cold reflection with various prescriptions. For the models below, we list the best-fit parameter values in Table 3 (“Nucleus Only”) and show the resulting data-to-model residuals in Figure 6. Fitting the `pexmon` model (model P in Table 2) yielded  $\chi^2_\nu = 1.60$  for  $\nu = 1471$  in the 0.5–9 keV range. The best-fit redshifts for the neutral and ionized lines were  $0.00392 \pm 0.0004$  and  $0.00371 \pm 0.00008$ , respectively, while the best-fit power law index, Fe abundance, and normalizations were  $\Gamma = 2.46^{+0.24}_{-0.24}$ ,  $Z_{\text{Fe}} = 4.5^{+1.1}_{-0.6}$ ,  $A_{\text{cold}} = (8.9^{+5.0}_{-0.5}) \times 10^{-2}$ , and  $A_{\text{warm}} = (2.8 \pm 0.2) \times 10^{-4}$  (both in units of photons  $\text{keV}^{-1} \text{ cm}^{-2} \text{ s}^{-1}$  at 1 keV), respectively. The power law slope is poorly constrained due to parameter limitations of the `pexmon` model.

We also fit the cold reflection with the `MYTorus` model in two distinct configurations (models M1 and M2 in Table 2). The first (M1) is a standard coupled configuration, wherein the neutral hydrogen column densities  $N_{\text{H}}$ , intrinsic power law slopes  $\Gamma$ , inclination angles  $\theta_{\text{inc}}$ , and normalizations of the `MYTZ` ( $A_{\text{pow}}$ ), `MYTS` ( $A_{\text{MYTS}}$ ), and `MYTL` ( $A_{\text{MYTL}}$ ) components are tied and fit together self-consistently to model a uniform torus geometry. The second (M2) is a decoupled configuration that employs two Compton scatterers, one edge-on and one face-on, where the corresponding normalizations for the different angles (e.g.,  $A_{\text{MYTS},90}$  and  $A_{\text{MYTS},00}$ ) vary independently, but the continuum and line components of a given angle are fixed as in model M1. This corresponds to a patchy torus whereby a portion of the Compton-scattered photons that “reflect” off the facing side of background clouds can bypass clouds that obscure photons along our direct line of sight (more details can be found in Yaqoob 2012, and we refer interested readers particularly to their Figure 15).

Fitting model M1 yielded  $\chi^2_\nu = 1.64$  for  $\nu = 1472$  in the 0.5–9 keV range. The best-fit redshifts for the neutral and ionized lines were  $0.00391 \pm 0.0004$  and  $0.00373 \pm 0.00008$ , respectively, while the best-fit power law index, scattering-to-line component (S/L) ratio,<sup>36</sup>  $\Gamma = 1.40^{+0.12}_{-0.08}$ , S/L ratio =  $0.42^{+0.12}_{-0.08}$ ,  $A_{\text{MYTS,cold}} = 7.4^{+2.9}_{-1.8}$ , and  $A_{\text{warm}} = (2.63^{+0.3}_{-0.3}) \times 10^{-4}$  (both in units of photons  $\text{keV}^{-1} \text{ cm}^{-2} \text{ s}^{-1}$  at 1 keV), respectively. Meanwhile, model M2 yielded  $\chi^2_\nu = 1.62$  for  $\nu = 1471$  in the 0.5–9 keV range, with best-fit power law index, scattering-to-line component ratio, and normalizations of  $\Gamma = 2.60^{+0.19}_{-0.19}$ , S/L ratio =  $0.67 \pm 0.09$ ,  $A_{\text{MYTS},00} = 0.19^{+0.01}_{-0.07}$ ,  $A_{\text{MYTS},90} = 0.00^{+1.74}_{-0.00007}$ , and  $A_{\text{warm}} = (4.1 \pm 0.2) \times 10^{-4}$  (all in units of photons  $\text{keV}^{-1} \text{ cm}^{-2} \text{ s}^{-1}$  at 1 keV), respectively. As before, the power law slope is not well-constrained over this particular energy range due to parameter limitations of the `MYTorus` model.

Finally, we fit the cold reflection with the `torus` model (model T in Table 2). The best fit yielded  $\chi^2_\nu = 1.65$  for  $\nu = 1472$  in the 0.5–9 keV range. The best-fit redshifts for the neutral and ionized lines were  $0.00363^{+0.0004}_{-0.0003}$  and  $0.00370^{+0.00009}_{-0.00007}$ , respectively, whereas the best-fit power law index, opening angle, and normalizations were  $\Gamma = 1.30^{+0.09}_{-0.05}$ ,  $\theta_{\text{open}} = 67^{+12}_{-15} \text{ deg}$ ,  $A_{\text{cold}} = (2.6^{+0.8}_{-0.5}) \times 10^{-2}$ , and  $A_{\text{warm}} = (3.0 \pm 0.2) \times 10^{-4}$  (both in units of photons  $\text{keV}^{-1} \text{ cm}^{-2} \text{ s}^{-1}$  at 1 keV), respectively. We note that the relatively low  $\Gamma$  value

<sup>36</sup> That is, the ratio of the  $A_{\text{MYTS}}$  to  $A_{\text{MYTL}}$  normalizations.

and small errors are largely dictated by the Fe lines, because there is no way to change the Fe line to continuum ratio through a metallicity parameter for this model.

As can be seen from Figure 6 and Table 3, all of the models are able to fit the 0.5–9 keV nucleus spectra equally well, with only very mild deviations in the residuals between them. In all cases, the residuals are almost exclusively due to low-level line emission (i.e., the strong ratio outliers in the lower panels of Figure 6), most of which is below 2 keV, which remains unaccounted for despite modeling  $\approx 90$  emission lines. We found that these residuals bias the relative normalization of the `bremss` component downward by  $\approx 20\%$ , but do not appear to significantly affect the `bremss` temperature or normalizations of the higher-energy components (this holds for all cold reflection models). Notably, there are wide variations in the power law slopes between models, which should be constrained better upon incorporating the  $>10$  keV data. If we limit the fit to the 2–9 keV spectra and fix the `bremss` and `tbabs` components, the  $\chi^2_\nu$  values drop to  $\approx 1$  and the photon indices become significantly harder ( $\Gamma \approx 1.4$ – $1.5$ ) in all cases, leading to decreased fractional contributions from the cold reflection in the 2–10 keV band. In the case of model M2, the 2–9 keV fit led to a reversal in the dominant cold reflection component from  $0^\circ$  to  $90^\circ$ . These large swings primarily demonstrate that the spectral properties of the cold and warm reflection are poorly constrained by the  $<10$  keV data alone, even when high signal-to-noise and well-resolved emission lines can be fit.

#### 4.2.2. Diffuse Emission and Point Source Contamination from Host Galaxy

Both extended and off-nuclear point source emission are evident in the *Chandra* images, particularly along the direction of the AGN radio jet and counter jet (see Figure 1). We modeled this emission in the *Chandra* ACIS-S data with several components to reproduce the main features in the galaxy, noting in particular that there are several key spectral signatures present in the nuclear spectra, which are also prevalent in the host spectrum.

First, we include in the host galaxy model an absorbed power law with slope  $\Gamma_{\text{pnt}}$  to account for the combined emission from extranuclear point sources, which we constrain separately below. A composite *Chandra* ACIS-S spectrum of all of the point sources together is shown in Figure 7 (green data and model). There are some notable bumps in the soft portion of the spectrum, which could either be intrinsic, or more likely are produced by poor background subtraction due to an inhomogenous extended emission component. As such, we fitted this spectrum only above 1.5 keV with a single cutoff power law model. Unfortunately, the limited 0.5–9 keV energy range is not sufficient to unambiguously determine the average spectrum slope, high-energy cutoff, and normalization of the host galaxy XRB population. Following Swartz et al. (2004) and Walton et al. (2011), we assume that NGC 1068 hosts an ultraluminous X-ray source (ULX) population and that emission characteristic of this population likely dominates the point-source emission. Recent evidence from *NuSTAR* (e.g., Baccetti et al. 2013; Walton et al. 2013, 2014; Rana et al. 2015) suggests that ULXs exhibit relatively hard spectra with spectral turnovers between 6 and 8 keV, and thus we adopt fixed values of  $\Gamma = 1.2$  and  $E_c = 7$  keV to represent the composite ULX-like spectrum. With these values, the normalization of the power law is  $8.9 \times 10^{-5}$  photons  $\text{keV}^{-1} \text{cm}^{-2} \text{s}^{-1}$  at 1 keV.

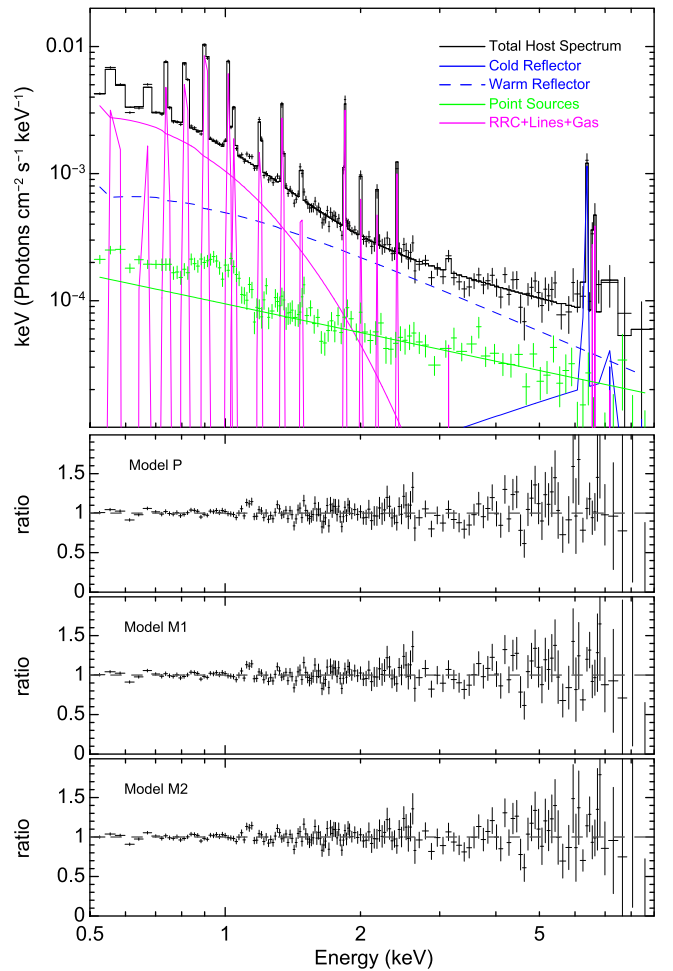


**Figure 7.** Total ACIS-S “host” unfolded spectrum (black) of all extranuclear emission extracted from a  $2''$ – $75''$  annulus centered on the nucleus of NGC 1068. The host spectrum is fitted with four models composed of partially absorbed cold and warm reflectors (blue solid and dashed lines, respectively), as well as RRC and the most prominent line components as identified by K14 (magenta solid lines) and the composite contribution from extranuclear point sources (green solid line). The top panel shows the fit to model P, while the rest of the panels show the data-to-model ratios for models P, M1, and M2, respectively. The top panel also shows the composite ACIS-S extranuclear point-source spectrum (green), which is modeled above 1.5 keV as a  $\Gamma_{\text{ULX}} = 1.2$  power law with a  $E_c = 7$  keV exponential cutoff rollover.

This component makes only a relatively small contribution to the overall host contamination in the 1.5–9.0 keV ( $\approx 25\%$ ) range, and quickly becomes negligible above 15 keV. We fixed the normalization of this fit and added the fixed ULX-like component to the overall host model.

At soft energies, we still see signs of extended RRC and line emission, which we again model as a  $kT_{\text{bremss}} = 0.31^{+0.01}_{-0.01}$  keV bremsstrahlung component (`bremss`,  $A_{\text{bremss}} = 0.0168^{+0.0004}_{-0.0003} \text{cm}^{-2}$ ) plus a subset of the 20 strongest emission lines found in the nuclear spectra; at the spectral resolution of ACIS-S, these 20 lines were sufficient to model nearly all of the spectral deviations from a smooth continuum. There may also be a contribution from hot gas associated with star formation, but since our main focus is to derive an empirical model to describe the soft emission, we simply absorb this into the normalization for the bremsstrahlung plus line emission model. The character of the ionized lines differs from those found in the nucleus spectrum, in the sense that lower ionization line species such as

S, Si, Mg are stronger in the host spectra relative to the ionized Fe lines, as might be expected for a UV/X-ray radiation field that is radiating from the central SMBH.

At hard energies, we additionally see traces of warm and cold AGN reflection as extended emission, which we model as a scattered power law and Compton-scattered continuum plus neutral lines, respectively. We continue to model the latter with either the `pexmon` or `MYTS+MYTL`; we do not fit the `torus` model because one cannot explicitly separate out the transmitted component.<sup>37</sup> As before, we assume that the warm and cold reflection components result from the scattering of the same direct transmitted power law (`cutoffpl`) with slope  $\Gamma_{\text{nuc}}$  and exponential cutoff rollover energy  $E_{c,\text{nuc}}$ , which is absorbed along the line of sight by a Compton-thick absorber (e.g., an edge-on torus). As before, we fixed the quantities  $E_{c,\text{nuc}} = 500$  keV,  $\theta_{\text{inc}} = 90^\circ$ , and  $N_{\text{H}} = 10^{25}$  cm<sup>-2</sup>, because these are poorly constrained by the <10 keV data alone.

Finally, we note that the absorption toward the counter jet region is significantly stronger than that toward the jet region, so we initially fit all the components to the jet and counter jet regions, allowing only for the  $N_{\text{H}}$  of the cold absorber to vary between them. This fit produced  $N_{\text{H}} = 3.1 \times 10^{20}$  cm<sup>-2</sup> toward the jet, which is consistent with the Galactic column, and  $N_{\text{H}} = 2.4 \times 10^{21}$  cm<sup>-2</sup> toward the counter jet. As such, the 2''–75'' host region was modeled through a layer of cold Galactic absorption (`tbabs`) and a cold partial coverer (`pcfabs`) with  $N_{\text{H}} = 2.4 \times 10^{21}$  cm<sup>-2</sup> and covering fraction of 50%. For all the models, we list the best-fit parameter values in Table 3 (“Host Only”) and show the resulting data-to-model residuals in Figure 7.

Fitting the `pexmon` (P) version of our host model yielded  $\chi^2_\nu = 1.42$  for  $\nu = 163$  in the 0.5–9 keV range. Given the quality and spectral resolution of the ACIS-S spectrum, we fixed the redshift at 0.00379. The best-fit power law index, Fe abundance, and normalizations were  $\Gamma = 2.49_{-0.25}^-$ ,  $Z_{\text{Fe}} = 43_{-19}^-$ ,  $A_{\text{cold}} = (2.5_{-0.5}^{+0.4}) \times 10^{-2}$  and  $A_{\text{warm}} = (6.7_{-0.2}^{+0.2}) \times 10^{-4}$  (both in units of photons keV<sup>-1</sup> cm<sup>-2</sup> s<sup>-1</sup> at 1 keV), respectively. It is worth noting here that the abundance value, albeit poorly constrained, is exceptionally high and probably highlights a critical breakdown of the model in this regime rather than an extreme intrinsic value. We also fit the host spectrum with the `MYTorus` (M1 and M2) versions of our host model. Fitting model M1 produced  $\chi^2_\nu = 1.44$  for  $\nu = 163$  in the 0.5–9 keV range. The best-fit power law index, scattering-to-line component ratio, and normalizations were  $\Gamma = 2.55_{-0.06}^-$ , S/L ratio of  $2.46_{-1.01}^{+3.49}$ ,  $A_{\text{MYTS,cold}} = 1.2_{-0.7}^{+0.8}$  and  $A_{\text{warm}} = (6.8_{-0.2}^{+0.2}) \times 10^{-4}$  (both in units of photons keV<sup>-1</sup> cm<sup>-2</sup> s<sup>-1</sup> at 1 keV), respectively. Meanwhile, model M2 yielded  $\chi^2_\nu = 1.46$  for  $\nu = 162$  in the 0.5–9 keV range, best-fit power law index, scattering-to-line component ratio, and normalizations were  $\Gamma = 2.56_{-0.05}^-$ , S/L ratio of  $2.25_{-0.90}^{+2.65}$ , and  $A_{\text{MYTS,00}} = (1.7_{-1.1}^{+1.1}) \times 10^{-2}$ ,  $A_{\text{MYTS,90}} = 0.00_{-1.58}^{+1.58}$ ,  $A_{\text{warm}} = (6.7_{-0.2}^{+0.2}) \times 10^{-4}$  (all in units of photons keV<sup>-1</sup> cm<sup>-2</sup> s<sup>-1</sup> at 1 keV), respectively. We note that the reflection component from the host emission should be composed almost exclusively of inclination 0° (“far-side, face-on”) reflection spectra whose line of sight does not intercept any torus material (see further discussion in Yaqoob 2012); thus we can effectively neglect the 90° component all together.

<sup>37</sup> The `torus` transmitted component could be made negligible by increasing the column density to  $10^{26}$  cm<sup>-2</sup>, but this would mean we would have to model all clouds as extremely Compton-thick, which is a major limitation.

Similar to the nucleus fits, the power law slopes for models P, M1, and M2 were not well-constrained due to parameter limitations of the various models and data bandpass limitations. The bulk of the residuals arise from unaccounted for line emission below 2 keV. As seen in Table 3, when we fit the models to the <2 keV spectrum and fix the bremsstrahlung component, the  $\chi^2_\nu$  values drop considerably for all models.

#### 4.2.3. Empirical Constraints on Extended Fe Line Emission

An alternative, more empirical approach can be made to understand the contribution from extended cold and warm reflection. For this, we simply measure the line fluxes from the two strongest tracers, the fluorescent Fe K $\alpha$  line and the ionized Fe He-like line, respectively. For simplicity, we use the M04a model (although we replace `pexmon` by `pexrav` in order to remove emission lines from the model) to estimate the continuum in both the *Chandra* HETG nuclear and ACIS-S host spectra, and then model the remaining lines with Gaussians as in Section 4.1. The line fluxes from the nuclear and host spectra are shown in Table 4 alongside the total line fluxes measured from the pn spectra. Reassuringly, the sum of the nuclear plus host are consistent with the total line fluxes, at least when we factor in statistical errors and cross-calibration differences.

After we account for contributions from the extended wings of the PSF using simulations from the `MARX`<sup>38</sup> ray-trace simulator (v4.5; Wise et al. 1997), we find that the extended Fe K $\alpha$  emission beyond 2'' (>140 pc) comprises 28 $_{-8}^{+8}$ % of the total. If the torus size is of order  $\approx 4$ –10 pc, then we should probably consider the extended fraction to be a lower limit to the cold reflection contribution from extended (i.e., non-torus) clouds, because there are likely to be contributions from similar material at 10–140 pc. Making a similar calculation for the ionized Fe He-like line, we find an extended fraction of 24 $_{-20}^{+18}$ %.

#### 4.2.4. Combined Fit

We now combine the models of the nucleus and host galaxy from the *Chandra* spectra to fit the total spectra from *NuSTAR*, *XMM-Newton*, and *Swift* BAT. As highlighted previously, the emission below  $\approx 2$  keV is dominated by the numerous line and bremsstrahlung components, and thus does not provide much constraint on the properties of the reflectors. At the same time, it contributes substantially to  $\chi^2$ , so for the remainder of the modeling we only consider the data above 2 keV. All the spectral components that are well-constrained by the previous nuclear and host spectral fitting, such as the extranuclear point source, RRC, and line emission, are fixed, because we are primarily concerned with constraining the relative contributions from the warm and cold reflection, as well as any potential direct AGN continuum. For modeling simplicity, we also chose to ignore the regions between 2.3–2.5 keV and 6.5–6.8 keV, which correspond to regions of ionized Si and Fe line emission, respectively; these regions always have considerable residuals that are not modeled by the continuum reflection components, but bias the component normalizations during the fitting process. We assume in the following that all components share a single intrinsic power law slope and any transmitted component, if present, must arise only from the nuclear portion

<sup>38</sup> <http://space.mit.edu/cxc/marx/>

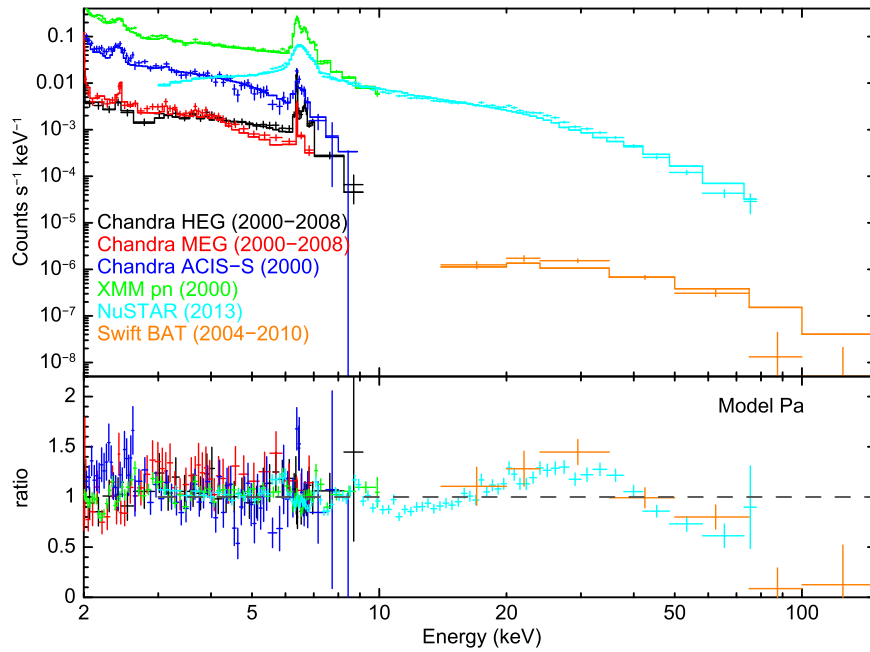


**Figure 8.** Top panel shows the final selection of X-ray spectra for NGC 1068 that we fitted from *NuSTAR* FPMA/FPMB (cyan), *XMM-Newton* pn (green), *Chandra* HEG/MEG (black/red), *Chandra* ACIS-S (blue), and *Swift* BAT (orange), all modeled with the best-fit parameters from model Pa; the bottom panel shows the data-to-model ratios for each spectrum. As in Figure 2, the overall consistency between the various data sets is good, once known normalization offsets are accounted for. In particular, the sum of the *Chandra* HEG/MEG (“Nucleus only”) and ACIS-S (“Host only”) models provides an excellent fit to the other (“Total”) data sets, where they overlap in energy. The only discrepancy between data sets appears to be a broad deficiency between 5.5 and 6.1 keV for the *NuSTAR* data. Model Pa is similar in shape to the M04a model, which still provides a poor fit to the data near the rise and peak of the Compton reflection hump. The HETG spectra are rebinned for presentation purposes.

of the spectrum. For selected relevant models below, we list the best-fit parameter values in Table 3 (“Total”) and/or plot their residuals in Figures 8–11.

**Model P.** We begin by fitting model P to the combined 2–195 keV spectra of NGC 1068. We fit  $\Gamma$  and  $Z_{\text{Fe}}$ , as well as the normalizations  $A_{\text{cold,nuc}}$ ,  $A_{\text{cold,host}}$ ,  $A_{\text{warm,nuc}}$ , and  $A_{\text{warm,host}}$  as free parameters, while we fix  $\theta_{\text{inc}} = 85^\circ$ ,  $E_c = 500$  keV, and  $N_{\text{H}} = 10^{25} \text{ cm}^{-2}$ . This model, hereafter “Pa,” yielded a poor fit, with  $\chi_\nu^2 = 1.34$  for  $\nu = 1666$ . The Pa model residuals, which are shown in Figure 8, highlight a general problem with fitting the spectral shape above 8 keV that we encountered with many of the adopted models, namely that the models either fit the spatially resolved  $<10$  keV data well but present clear  $>10$  keV residuals, or vice versa. Allowing the cutoff energy to vary failed to yield any improvement in  $\chi_\nu^2$ , with a best-fit value of  $E_c = 500_{-176}^{+176}$  keV, hereafter model “Pb.” Alternatively, also allowing the inclination angle to vary to  $\theta_{\text{inc}} = 24_{-5}^{+7}$  deg, hereafter model “Pc,” significantly improved the fit, with a new  $\chi_\nu^2 = 1.28$ . We note that this inclination angle suggests a face-on configuration, perhaps indicative of scattering off the back wall of a fiducial torus, while the best-fit photon index ( $\Gamma = 1.65 \pm 0.02$ ) is somewhat lower than one would expect for such a high accretion rate source like NGC 1068 (e.g.,  $\Gamma = 2.5$ ; Fanali et al. 2013). Critically, although the high-energy residuals have improved, significant deviations of the form shown in Figure 8 from the observed continuum shape still remain. Again, varying the cutoff energy to  $E_c = 387_{-176}^{+176}$  keV fails to yield any substantial improvement in  $\chi_\nu^2$ .

**Model M1.** We now turn to the cold reflection as modeled by MYTORUS. As before, we initially adopt a “standard” fully coupled, uniform torus geometry, hereafter “M1a.” While there is no physical reason for the nuclear and extended components

to be the same, we begin with such a scenario because it represents how previous studies would model the entire *XMM-Newton* or *NuSTAR* spectrum. For the M1a model, we fit  $\Gamma = 1.40_{-0.09}^{+0.09}$  and the component normalizations, and fix the other parameters to  $N_{\text{H}} = 10^{25} \text{ cm}^{-2}$ ,  $\theta_{\text{inc}} = 90^\circ$ ,  $E_{\text{cut}} = 500$  keV, and the S/L ratio to 1. Aside from allowing the reflection component normalizations to vary, the properties of the nucleus and host reflectors were tied together. The resulting fit was poor, with  $\chi_\nu^2 = 3.78$  for  $\nu = 1666$ , and large residuals around both the neutral Fe  $K\alpha$  line and to a lesser extent the Compton hump. Moreover, the power law slope is quite flat. From the residuals, it is clear that an S/L ratio of 1 is insufficient, and allowing the S/L ratio to vary to  $26.7_{-1.0}^{+14.2}$ , hereafter “M1b,” substantially improved the fit with  $\chi_\nu^2 = 1.78$ . Such an S/L ratio is unreasonably high, however, and implies that the adopted values for some of the fixed parameters are likely wrong. Varying  $E_{\text{cut}}$  to  $55_{-5}^{+4}$  keV (“M1c”) lowered the S/L ratio to  $15.0_{-0.9}^{+1.2}$  and resulted in  $\chi_\nu^2 = 1.61$ . Finally, further varying the inclination angle and column density improves the fit to  $\chi_\nu^2 = 1.31$ , with  $\Gamma = 1.40_{-0.12}^{+0.12}$ ,  $N_{\text{H}} = (9.4_{-3.3}^{+3.3}) \times 10^{24} \text{ cm}^{-2}$ ,  $\theta_{\text{inc}} = 78_{-4}^{+3}$ ,  $E_{\text{cut}} = 41_{-4}^{+5}$  keV, and an S/L<sub>nuc+host</sub> ratio of  $3.8_{-0.8}^{+0.5}$  (hereafter “M1d”). This last model fits the  $>10$  keV continuum significantly better, but at the expense of producing residuals in the  $<10$  keV continuum (see Figure 9), while retaining a flat power law slope. Ultimately, we conclude that none of the coupled MYTORUS models provides a reasonable fit to the continuum shape. It is important to point out that if we had only modeled either the  $<10$  keV spectra or the total aperture spectra, we would have arrived at a satisfactory  $\chi_\nu^2$ .

As an alternative to the fully coupled models, we tried fitting separate MYTUS+MYTL parameters for the nucleus and the host spectra, as might be expected for the combination of a thick

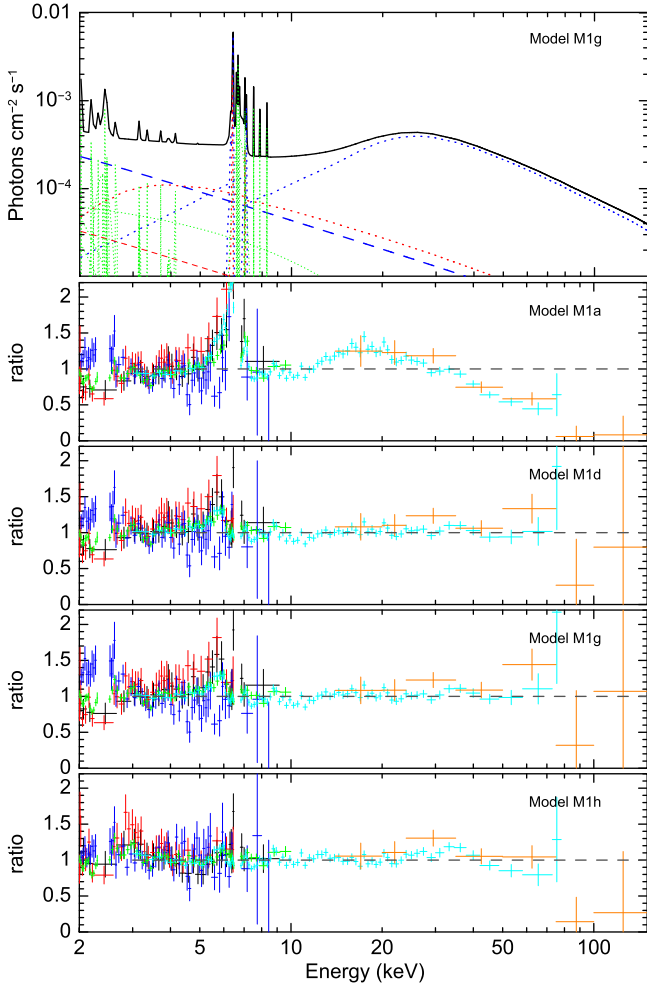


**Figure 9.** *Top panel:* model M1g shown for the full data set. Solid lines denote the overall spectrum. Blue lines represent the nuclear warm (dashed) and cold (dotted) reflection components. The red lines represent the host warm (dashed) and cold (dotted) reflection components. The RRC and line emission components for both the nuclear and host models are shown as dotted green lines. *Bottom panels:* data-to-model ratios for several M1 models, with the same color-coding as Figure 8. Many of the models we fit exhibited poor fits to the data either above or below 10 keV. The HETG spectra are rebinned for presentation purposes.

torus and more tenuously distributed larger-scale molecular clouds, which have been found from mid-IR constraints on NGC 1068. We began by fitting a single photon index  $\Gamma = 1.80^{+0.05}_{-0.07}$ , the various component normalizations, and independent column densities  $N_{\text{H,nuc}} = (9.8^{+0.2}_{-0.2}) \times 10^{24} \text{ cm}^{-2}$  and  $N_{\text{H,host}} = (2.4^{+0.1}_{-0.2}) \times 10^{23} \text{ cm}^{-2}$ , and S/L ratios  $12.2^{+1.8}_{-1.9}$  and  $0.5^{+0.3}_{-0.2}$  for the nucleus and host components, respectively, while fixing  $\theta_{\text{inc}} = 90^\circ$  and  $E_{\text{cut}} = 500 \text{ keV}$  (hereafter “M1e”). This fit produced  $\chi^2_\nu = 1.54$  for  $\nu = 1663$ . Allowing  $E_{\text{cut}} = 33^{+5}_{-3} \text{ keV}$  improved the fit to  $\chi^2_\nu = 1.30$ , with modest changes to the other free parameters such that  $\Gamma$  remained pinned at its minimum, while  $N_{\text{H,nuc}} = (5.3^{+0.4}_{-0.5}) \times 10^{24} \text{ cm}^{-2}$ ,  $N_{\text{H,host}} = (0.09 \pm 0.03) \times 10^{24} \text{ cm}^{-2}$ ,  $S/L_{\text{nuc}} = 10.8^{+1.3}_{-0.8}$ , and  $S/L_{\text{host}} = 1.0^{+0.4}_{-0.2}$  (hereafter “M1f”). Finally, allowing the inclination angles to vary (hereafter “M1g”) only marginally improves the fit to  $\chi^2_\nu = 1.28$ , with free parameters  $\Gamma = 1.40^{+0.34}_{-}$ ,  $E_{\text{cut}} = 34^{+58}_{-4} \text{ keV}$ ,  $N_{\text{H,nuc}} = (8.0^{+1.6}_{-1.6}) \times 10^{24} \text{ cm}^{-2}$ ,  $N_{\text{H,host}} =$

$(1.3^{+1.5}_{-0.9}) \times 10^{24} \text{ cm}^{-2}$ ,  $S/L_{\text{nuc}} = 3.5^{+0.8}_{-0.5}$  and  $S/L_{\text{host}} = 1.5 \pm 0.3$ .

We note that freeing the column density and normalization toward the transmitted component (hereafter “M1h”) to  $N_{\text{H,trans}} = (6.0^{+1.3}_{-0.8}) \times 10^{24} \text{ cm}^{-2}$  resulted in  $\chi^2_\nu = 1.13$ , with best-fit values of  $\Gamma = 2.20^{+0.07}_{-0.12}$ ,  $E_{\text{cut}} = 72^{+75}_{-21} \text{ keV}$ ,  $N_{\text{H,nuc}} = (2.6^{+0.5}_{-0.5}) \times 10^{23} \text{ cm}^{-2}$  and  $N_{\text{H,host}} = 10^{25} \text{ cm}^{-2}$  (unconstrained),  $S/L_{\text{nuc}} = 1.0^{+0.2}_{-0.3}$  and  $S/L_{\text{host}} = 2.0^{+0.6}_{-0.6}$ , and inclination angles of  $0.7^{+4.5}_{-}$  deg and  $1.9^{+10.5}_{-}$  deg for the nucleus and host components, respectively. This model is the best version of the “standard” MYTORUS configuration and crudely models the key continuum and line features, but ultimately predicts that NGC 1068 should be dominated by the transmitted component above 20 keV. The normalizations of the various continuum components are  $A_{\text{trans}} = 2.6^{+1.3}_{-1.3} \times 10^{-4}$ ,  $A_{\text{warm,nuc}} = (3.0^{+1.3}_{-1.3}) \times 10^{-4}$ ,  $A_{\text{cold,nuc}} = (4.0^{+0.7}_{-0.5}) \times 10^{-2}$ ,  $A_{\text{warm,host}} = (3.9^{+1.5}_{-1.4}) \times 10^{-4}$ , and  $3A_{\text{cold,host}} = (9.4^{+4.2}_{-3.7}) \times 10^{-3}$ , respectively (all in units of photons  $\text{keV}^{-1} \text{ cm}^{-2} \text{ s}^{-1}$  at 1 keV), implying a covering fraction of  $\sim 0.008$  and  $\sim 0.002$  for the nucleus and host cold reflection components. Such low-covering fractions run contrary to the variability constraints presented in Sections 2.1 and 2.6. As such, the good fit appears to be a consequence of allowing freedom for several spectral components to fit small portions of the overall spectrum, and is presumably degenerate in this sense.

We conclude that the “standard” configuration of MYTORUS has considerable difficulty reproducing the main spectral and temporal X-ray characteristics of NGC 1068.

*Model M2.* We now turn to the second MYTORUS configuration, which employs two MYTORUS Compton scatterers fixed at  $0^\circ$  and  $90^\circ$ , representing a potential clumpy torus-like distribution. Following the discussion in Section 4.2.2, we only invoke the  $0^\circ$  component to fit the host spectrum. We began by fitting a basic form of this model, hereafter “M2a,” with varying  $\Gamma = 2.29^{+0.04}_{-0.02}$  and component normalizations, with the remaining parameters fixed to  $N_{\text{H}} = 10^{25} \text{ cm}^{-2}$ ,  $S/L_{\text{nuc+host}} = 1.0$ , and  $E_{\text{cut}} = 500 \text{ keV}$  for all scattering components. The best fit returns  $\chi^2_\nu = 1.84$  for  $\nu = 1666$ , which is a significant improvement over model M1a. However, the continuum is still not well fit, and the best fit  $A_{\text{nuc,MYTS,90}}$  normalization is consistent with zero ( $< 1\%$  of cold reflector flux). Fitting the  $S/L_{\text{nuc+host}}$  ratio to  $4.3^{+0.4}_{-0.3}$  (hereafter “M2b”) reduces  $\chi^2_\nu = 1.51$ , and yields  $\Gamma = 1.49 \pm 0.04$  plus moderate variations in the component normalizations. M2b offers a significant improvement over model M1b. Additionally, varying  $E_{\text{cut}} = 146^{+76}_{-50} \text{ keV}$  (hereafter “M2c”), provides only very marginal improvement ( $\chi^2_\nu = 1.48$ ) and leaves the parameters largely unmodified. Finally, varying the three column densities (hereafter “M2d”) improves the fit to  $\chi^2_\nu = 1.14$ , with  $\Gamma = 2.10^{+0.06}_{-0.07}$ , an  $S/L_{\text{nuc+host}}$  ratio of  $1.0 \pm 0.1$ ,  $E_{\text{cut}} = 128^{+115}_{-44} \text{ keV}$ ,  $N_{\text{H,nuc,90}} = (10.0^{+4.4}_{-4.4}) \times 10^{24} \text{ cm}^{-2}$ ,  $N_{\text{H,nuc,0}} = (1.5 \pm 0.1) \times 10^{23} \text{ cm}^{-2}$ ,  $N_{\text{H,host,0}} = (5.0^{+4.5}_{-1.9}) \times 10^{24} \text{ cm}^{-2}$ , and normalizations of  $A_{\text{warm,nuc}} = (2.5^{+0.3}_{-0.4}) \times 10^{-4}$ ,  $A_{\text{cold,nuc,90}} = (3.0^{+0.5}_{-0.5}) \times 10^{-1}$ ,  $A_{\text{cold,nuc,0}} = (3.6^{+0.3}_{-0.2}) \times 10^{-2}$ ,  $A_{\text{warm,host}} = (3.4^{+0.3}_{-0.4}) \times 10^{-4}$ ,  $A_{\text{cold,host,0}} = (1.0^{+0.2}_{-0.2}) \times 10^{-2}$  (all in units of photons  $\text{keV}^{-1} \text{ cm}^{-2} \text{ s}^{-1}$  at 1 keV). Freezing the high-energy cutoff at  $E_{\text{cut}} = 500 \text{ keV}$  (hereafter “M2e”) leaves the above parameters virtually unchanged and  $\chi^2_\nu = 1.16$ .

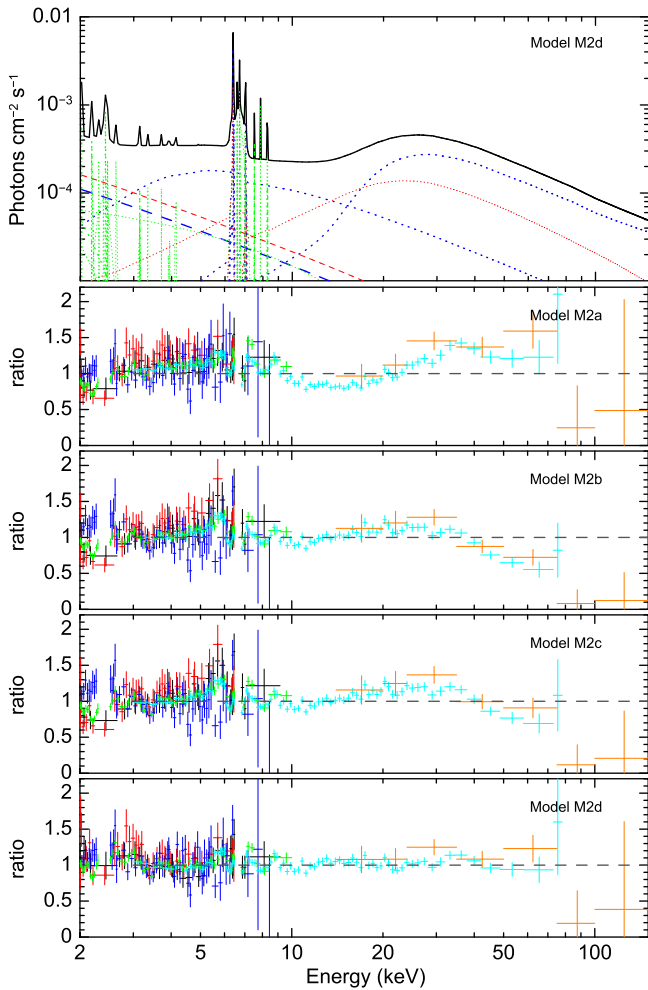


**Figure 10.** Same as Figure 9, but for M2 models. The model M2d provides the best overall fit to the spectra among all the models.

As can be seen in Figure 10, the data-to-model ratio residuals are now fairly flat out to  $\approx 80$  keV. The primary difference between model M2d (or M2e) and the others lies in how the nuclear  $\theta_{\text{inc}} = 0^\circ$  cold reflector component, due to its significantly lower  $N_{\text{H}}$ , is able to fill in the spectral gap around 4–8 keV between the “normal” cold and warm reflectors. One important aspect of this model that deserves to be highlighted is the fact that while the higher  $N_{\text{H}}$  component provides the bulk of the flux to the Compton hump, it does not contribute much to the Fe fluorescence line emission. Instead, the lower  $N_{\text{H}}$  component produces the bulk of the Fe fluorescence line emission, and dominates the continuum peaking around 5–10 keV. Thus, the two key features of Compton reflection, namely the hump and Fe line, need not arise from a single absorber and in fact likely arise from different obscuring clouds. Assuming a single absorber will likely lead to misinterpretations.

*Model T.* Finally, we fit the cold reflection with the `torus` model. As noted in Section 4.2, this model is not suitable for fitting the host spectrum, so we instead modeled the host spectrum identically to the M2 case using `MYTS` + `MYTL` components with an inclination angle of  $\theta_{\text{inc}} = 0^\circ$ . Varying  $\Gamma = 1.96^{+0.05}_{-0.04}$ ,  $\theta_{\text{open}} = 64^{+3}_{-2}$  deg, and component normalizations with fixed values of  $N_{\text{H}} = 10^{25} \text{ cm}^{-2}$ ,

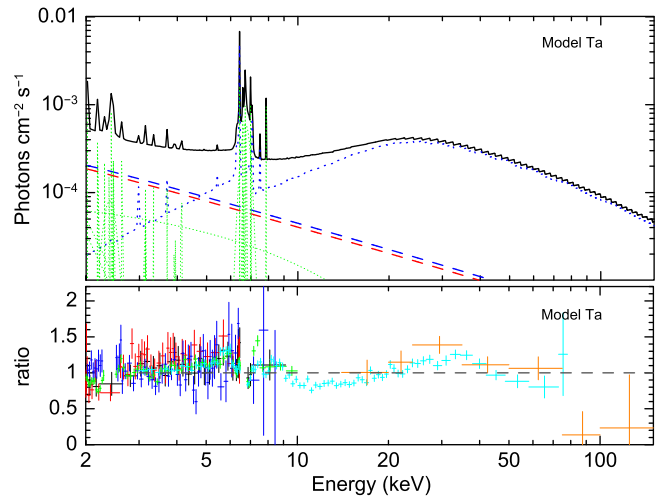


**Figure 11.** Same as Figure 9, but for T models.

$\theta_{\text{inc}} = 87^\circ$ ,  $E_{\text{cut}} = 500$  keV, and a  $S/L_{\text{host}}$  ratio of 1.0, yielded  $\chi^2_\nu = 1.61$  for  $\nu = 1666$  (hereafter “Ta”). This provides a relatively poor fit, with residuals near the Fe lines and  $>10$  keV continuum (Figure 11). Freeing the `torus` inclination angle to  $\theta_{\text{T,inc}} = 87^{+16}_{-16}$  (hereafter “Tb”) does not improve the fit. Further varying the nuclear and host column densities to  $N_{\text{H,nuc}} = (6.9^{+0.6}_{-0.8}) \times 10^{24} \text{ cm}^{-2}$ ,  $N_{\text{H,host,0}} = (10.0^{+6.6}_{-6.6}) \times 10^{24} \text{ cm}^{-2}$  (hereafter “Tc”) leads to a modest improvement of  $\chi^2_\nu = 1.57$ , with  $\Gamma = 2.13^{+0.04}_{-0.06}$ ,  $\theta_{\text{open}} = 69^{+4}_{-3}$  deg, and  $\theta_{\text{incl}} = 87^{+12}_{-12}$  deg. As with other models, there are significant residuals as the model fails to fit the continuum shape well. In all cases, the host cold reflection normalization is consistent with zero. It seems that the `torus` model does not provide enough flexibility to model the transmission and scattered components separately, and again we conclude that the `torus` model has considerable difficulty reproducing the main spectral X-ray characteristics of NGC 1068.

#### 4.2.5. Model Summary

We tested a few cold reflection models earlier in this section. As traditionally done, we modeled NGC 1068 with a single monolithic cold reflector using `pexmon` (models Pa–Pc), `MYTorus` (models M1a–M1d), and `torus` (models Ta–Tc). Alternatively, we also modeled NGC 1068 with multiple reflectors using two or three `MYTorus` components to fit the two spatially distinct nuclear and host regions (models M1e–M1h) and additional complexity in the nuclear spectrum (models M2a–M2d). We found that many are able to fit either the spatially resolved  $<10$  keV spectra or the total aperture spectra well, but generally not both.

The two models that do manage to fit all the spectra well are M1h and M2d. In both cases, a cold reflection component with  $N_{\text{H}} \sim 10^{23} \text{ cm}^{-2}$  peaking at 5–10 keV is required to fill in a critical gap in the model where the declining warm reflector and the increasing cold reflector meet. Model M1h is rejected, however, because it requires a strong transmitted component, which runs contrary to our variability results (Section 3), leaving only M2d as the preferred model.

When modeling M2d, we find a best-fit power law slope of  $\Gamma = 2.10^{+0.06}_{-0.07}$ , which is marginally higher than the average AGN value of  $\Gamma \sim 1.9$  (e.g., Reeves & Turner 2000). Notably, high  $\Gamma$  values are often associated with high Eddington ratio

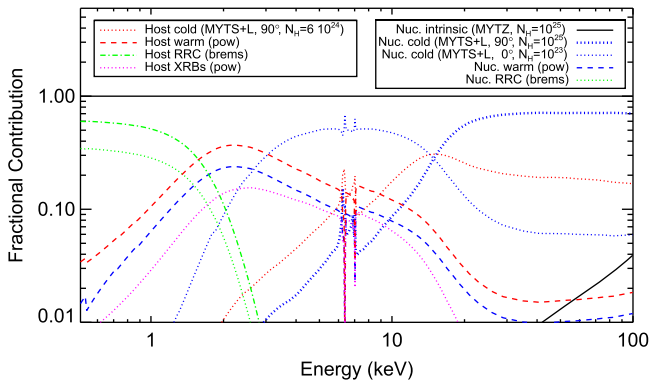


**Figure 12.** Fractional contributions from individual model M2d components. The black solid line denotes the intrinsic continuum (MYTZ component). Blue lines represent the nuclear warm (dashed) and cold (dotted;  $N_H = 10^{25} \text{ cm}^{-2}$  at  $90^\circ$  and  $N_H = 1.4 \times 10^{23} \text{ cm}^{-2}$  at  $0^\circ$ ) reflection components; the thicker line denotes the  $0^\circ$  model. Red lines signify the host warm (dashed) and cold (dotted;  $N_H = 5 \times 10^{24} \text{ cm}^{-2}$  at  $90^\circ$ ) reflection components. Green lines denote the RRC components for the nuclear (dotted) and host (dashed-dotted) models, respectively, while the ULX-like contribution is shown as the dotted magenta line. For clarity, we exclude the  $\approx 90$  Gaussian lines when calculating fractional contributions, as their presence dramatically shifts the continuum contributions over small portions of the spectrum. There are clear changes in the dominance of different continuum components as a function of energy.

systems (e.g., Shemmer et al. 2006; Risaliti et al. 2009; Brightman et al. 2013), and thus the slope is consistent with our initial accretion rate assessment in Section 1. The high-energy cutoff value for this model,  $E_{\text{cut}} = 128_{-44}^{+115}$  keV, is perhaps somewhat low. This could imply low coronal temperatures, although the error bars indicate this value is poorly constrained and should not be taken too seriously. With this model, we derive total observed X-ray luminosities of  $L_{2-10 \text{ keV, obs}} = 1.8 \times 10^{41} \text{ erg s}^{-1}$ ,  $L_{10-40 \text{ keV, obs}} = 5.6 \times 10^{41} \text{ erg s}^{-1}$ , and  $L_{1-200 \text{ keV, obs}} = 1.3 \times 10^{42} \text{ erg s}^{-1}$ , and intrinsic<sup>39</sup> X-ray luminosities of  $L_{2-10 \text{ keV, intr}} = 2.2 \times 10^{43} \text{ erg s}^{-1}$ ,  $L_{10-40 \text{ keV, intr}} = 1.5 \times 10^{43} \text{ erg s}^{-1}$ , and  $L_{1-200 \text{ keV, intr}} = 4.6 \times 10^{43} \text{ erg s}^{-1}$ , respectively. This intrinsic  $L_{2-10 \text{ keV}}$  value is only a factor of  $\approx 1.6$  lower than that predicted by the mid-IR to X-ray relation of Gandhi et al. (2009), despite the obvious spectral complexity that we find. Breaking down the percentage of spectral contributions to the total observed  $L_{1-200 \text{ keV, obs}}$ , gives intrinsic continuum (1.5%); nuclear cold reflection  $0^\circ$  (12.9%); nuclear cold reflection  $90^\circ$  (55.3%); nuclear warm reflection (3.1%); nuclear RRC + RL (3.1%); host cold reflection  $0^\circ$  (16.6%); host warm reflection (4.3%); host RRC + RL (2.1%); and host off-nuclear (1.5%). Figure 12 shows the fractional contributions from the main components of the M2d model. In total, these observed reprocessed components represent  $\approx 2.8\%$  of the estimated intrinsic 1–200 keV luminosity.

We stress that the scattered emission from NGC 1068 is clearly complex and thus the models attempted were by no means exhaustive. Alternative complex component combinations likely exist that can fit the obvious Compton hump and Fe fluorescence line, as well as strike a balance in the overall reflection continuum levels. Nonetheless, we can conclude that simple configurations such as a single nuclear reflector or a patchy torus fail to match the data, and an additional lower density scattering component is needed.

## 5. DISCUSSION

From the combined modeling we performed in the previous section, there are a few points worth stressing. The quality of the *NuSTAR* data plays an important role in constraining the fits. With poorer quality data, such as that from *Suzaku*, *BeppoSAX*, or *Swift* BAT shown in Figure 2, several of the models we considered produce acceptable fits. Only with the *NuSTAR* data can we observe in detail the nature of the rising Compton hump and broad peak, which is difficult to fit with a single cold reflection model. Likewise, fitting the *Chandra* nuclear and host spectra separately, we find that the combination of good-quality nuclear and host spectra creates considerable tension for several models that would otherwise fit the total *XMM-Newton* and *NuSTAR* spectra at acceptable levels. This study demonstrates that it is important to have both high-quality spectra above 10 keV and spatially resolved X-ray spectra in order to, e.g., reject simple monolithic cold reflection models. The analysis by Arévalo et al. (2014) of the Circinus Galaxy also benefited from the powerful combination of high-quality *NuSTAR* data and spatial separation of the nuclear and host components, demonstrating that a significant fraction of the warm and cold reflection components arise from  $>2''$  ( $>38 \text{ pc}$  at the distance of Circinus).

These two objects are among the closest and X-ray brightest Compton-thick AGN on the sky, and benefit from a wealth of high-quality X-ray data. Unfortunately, there are only a handful of nearby Compton-thick AGN where a similar analysis can be made, but it will be interesting to see how diverse parameter space might be with respect to this multiple cold reflector model. For fainter and more distant obscured X-ray AGN, however, we can only obtain modest-to-poor quality *NuSTAR* data. Moreover, with the angular resolution of currently available instruments, we will be unable to separate the 2–8 keV nuclear emission from its host. So while it may be possible to model the total emission from such AGN in reasonable detail and with acceptable results (e.g., Baloković et al. 2014; Del Moro et al. 2014; Gandhi et al. 2014; Lansbury et al. 2014; Brightman et al. 2015), it will not be possible to investigate the detailed physical properties of such sources, as for NGC 1068 and Circinus (Arévalo et al. 2014). The work here and in Circinus highlight the potential issues of modeling a total spectrum from, for example, *XMM-Newton* or *NuSTAR* with a monolithic model of the obscurer. For the multiple cold reflector model shown in Figure 10, different portions of the total reflection spectrum seen by *NuSTAR* and *XMM-Newton* appear to arise from different obscuring clouds, decoupling the two key features of cold reflection. The fact that cold reflectors occur on a variety of physical scales or with a variety of column densities is unlikely to change the basic requirement for a high column density associated with a mildly or heavily Compton-thick AGN. However, it is possible for this variety to change interpretations regarding the relative Fe abundance, inclination angle, covering factor for a given column density, and high-energy cutoff; we observed several of these to vary significantly from model to model in Section 4.2.

Although unobscured AGN are dominated by the transmitted power law, the Fe line and Compton hump do imprint themselves as secondary contributions. To test how our preferred model of NGC 1068 might affect the fitting of unobscured AGN, we inverted the inclination angles of the MYTorus components by  $90^\circ$  and added a relativistically blurred ionized disk reflection component (`relconv*xillver`;

<sup>39</sup> This does not include contributions from scattered components or contamination.

Dauser et al. 2013; García et al. 2014). We linked the disk reflection parameters to previously determined values (e.g.,  $\Gamma$ ,  $E_{\text{cut}}$ ,  $\theta_{\text{inc}}$ ,  $Z_{\text{Fe}}$ ), or fixed them to their default values. We normalized the disk reflection relative to the other components, such that it provides the same contribution at 30 keV as the combined cold reflection components. In this configuration, the relative total reflection flux is high, comprising  $\approx 30\%$  of the total at 30 keV, yet the narrow observed Fe  $K\alpha$  equivalent width (EW) is only 40 eV; the latter value is toward the low end of EW measurements made for Seyfert 1s (e.g., Yaqoob & Padmanabhan 2004) and implies that the narrow Fe  $K\alpha$  EW may not be a useful estimator for the relative strength of the cold reflection component, as is sometimes assumed, and even low EW Fe lines may signify important scattered-light contributions at higher energies.

We then varied the exponential cutoff energy for our unobscured version of NGC 1068 between three values (100, 300, and 500 keV). We simulated a 50 ks *NuSTAR* spectrum, resulting in  $\sim 10^6$  3–79 keV photons, and fit this with a model typical of those used in unobscured AGN studies (i.e., where the transmitted, disk reflection, and cold reflection are modeled as `cutoffpl+relcov*xillver+pexrav+zgauss`, respectively, and absorbed by a low column density `tbabsGal`). We allowed  $\Gamma$ ,  $E_{\text{cut}}$ ,  $Z_{\text{Fe}}$ , and the component normalizations to vary, and fixed the remaining parameters at typical values (e.g.,  $X_i = 3.1$ ,  $Z_{\text{Fe}} = 3$ ,  $a = 0.9$ ,  $\cos \theta_{\text{pexrav}} = 0.3$ ,  $\theta_{\text{xillver}} = 20^\circ$ ). In all cases, we obtained reasonable fits with  $\chi_\nu \approx 1.0$ –1.1 and found that the power law slope was consistent with its input value. For input  $E_{\text{cut}}$  values of 100, 300, and 500 keV, we obtained best-fit values of  $312_{-32}^{+43}$ ,  $227_{-16}^{+27}$ ,  $302_{-30}^{+37}$  keV, respectively, and  $Z_{\text{Fe}} = (0.7\text{--}0.8) \pm 0.1$ . We ran another simulation, naively assuming the M2d reflection components were globally the same, which yielded similar results for the cutoff energies. Such toy models are admittedly far from conclusive, due to the likely large number of permutations of possible spectral shapes of components and degeneracies among parameters, not to mention the manner in which we implemented the high-energy cutoff for `MYTORUS`. Nonetheless, they do highlight how errors on some quantities, such as the high-energy cutoff, could be underestimated even in unobscured AGN and can strongly depend on what model assumptions are adopted.

The best-fit model for the composite X-ray data set, M2d, could be visualized as follows. In the inner  $2''$  (140 pc) region, we see a  $\theta_{\text{inc}} = 90^\circ$  (fixed),  $N_{\text{H}} \approx 10^{25} \text{ cm}^{-2}$  reflector with a covering factor of 0.5 (fixed), which to first order is presumably associated with a standard, compact, torus-like structure. Additionally, we find a  $\theta_{\text{inc}} = 0^\circ$  (fixed),  $N_{\text{H}} \approx 10^{23} \text{ cm}^{-2}$  reflector with an estimated covering factor of 0.13, based on the relative component normalizations, which appears to act as a screen. This less dense component could be more or less co-spatial with the dense torus or it could be material in the ionization cone. In both cases, we might expect a stratification of dense material stemming from instabilities associated with the photoionization of the dense molecular gas by AGN radiation field structures (e.g., akin to the structures at the boundaries between H II regions and molecular clouds; see, for example, Pound 1998). Alternatively, it could simply be reflection from larger-scale interstellar clouds aggregating within the inner  $\approx 100$  pc (e.g., Molinari et al. 2011). In all cases, we should expect a range of clouds that follow a log-normal column density distribution (e.g., Lada et al. 1999;

Goodman et al. 2009; Lombardi et al. 2010; Tremblin et al. 2014). This should in turn introduce considerable complexity into the AGN reflection components. We appear to be seeing the first hints of this anticipated complexity in NGC 1068. We note that this less dense reflection component produces the bulk of the Fe  $K\alpha$  line emission and, moreover, we see no strong long-term variability from the  $< 10$  keV continuum or line flux. Thus, we conclude that this second reflection component likely arises light years from the central AGN and/or is distributed such that it washes out any variability.

We note that at a basic level, the above multi-component reflector configuration found in the nuclear region appears reasonably consistent with the picture stemming from mid-IR interferometry for NGC 1068 (e.g., Jaffe et al. 2004; López-Gonzaga et al. 2014), whereby a three-component model, composed of a small obscuring torus and two dusty structures at larger scales (at least 5–10 pc), best fits the data. The larger-scale dust is off-center and could represent the inner wall of a dusty cone (e.g., the ionization cone). Based on the compactness and detailed modeling of spectral energy distributions in various AGN, these structures are believed to be clumpy and composed of a range of torus clouds with column densities of  $N_{\text{H}} \sim 10^{22}\text{--}10^{23} \text{ cm}^{-2}$  (e.g., Elitzur & Shlosman 2006; Nenkova et al. 2008; Ramos Almeida et al. 2009).

On more extended ( $> 2''$ ) scales, we find an additional  $\theta_{\text{inc}} = 0^\circ$  (fixed),  $N_{\text{H}} \approx (4\text{--}10) \times 10^{24} \text{ cm}^{-2}$  reflector with a covering factor of 0.03. The inclination angle, if left free, is not strongly constrained, and thus it is not clear whether this component is a screen, a mirror, or perhaps both. This material could be associated with clumpy molecular clouds either within the ionization cone or the general interstellar cloud population in the host galaxy. Intriguingly, our separation of nuclear and host spectra was purely based on instrumental reasons, and thus, if the distribution of clouds is strongly centralized and goes roughly as  $1/r$  or  $1/r^2$  (e.g., Bally et al. 1988; Nenkova et al. 2008), we might expect at least a fraction of the Fe  $K\alpha$  line flux currently assigned to the  $N_{\text{H}} \approx 10^{25} \text{ cm}^{-2}$  torus-like nuclear reflection component to arise from reflection by extended material. This suggests that a non-negligible portion of the overall reflection component in NGC 1068 arises outside the torus. As we found in Section 4.2.3, the empirical fraction of extended Fe  $K\alpha$  flux is substantially higher ( $\approx 30\%$ ) than the estimate of the overall reflection, suggesting that perhaps there are also multiple  $N_{\text{H}}$  components responsible for the extended emission. Based on the same molecular cloud distribution argument as above, it may be possible for the majority of the narrow Fe  $K\alpha$  emission to originate from radii well beyond the classic torus.

## 6. CONCLUSIONS

We have characterized the X-ray spectra of the archetypal Compton-thick AGN, NGC 1068, using newly acquired *NuSTAR* data, combined with archival data from *Chandra*, *XMM-Newton*, and *Swift* BAT. We modeled NGC 1068 with a combination of a heavily obscured transmitted power law, scattering by both warm and cold reflectors, radiative recombination continuum and line emission, and off-nuclear point-source emission, employing a handful of cold reflector models. Our primary results can be summarized as follows:

1. The  $>10$  keV *NuSTAR* data are consistent with past measurements to within cross-calibration uncertainties, but provide at least an order of magnitude more sensitivity, allowing us to constrain the high-energy spectral shape of NGC 1068 in better detail than ever before. We find no strong evidence for short- or long-term variability, which is consistent with the primary transmitted continuum being completely obscured from our line of sight.
2. We use *Chandra* ACIS-S and HETG data to split the reflection-dominated spectrum of NGC 1068 into two spatial regimes representing the nuclear ( $<2''$ ) and host ( $2''$ – $75''$ ) contributions to the total spectrum measured by *NuSTAR*, *XMM-Newton*, and *Swift* BAT. Modeling reflection components from two distinct spatial regimes allows us to break previously unexplored degeneracies to aid physical interpretation.
3. Modeling NGC 1068 as a monolithic cold reflector with a single column density  $N_{\text{H}}$  generally fails to reproduce some critical portion of the combined spectra accurately, and/or yields parameters that are difficult to reconcile with robust independent observations, regardless of the Compton reflection model used.
4. Modeling NGC 1068 using a multi-component reflector (here as best-fit model M2d with two nuclear and one extended *MYTORUS* components with best-fit values of  $\Gamma \approx 2.1$ ,  $E_{\text{cut}} \gtrsim 90$  keV,  $N_{\text{H}} = 10^{25} \text{ cm}^{-2}$ ,  $N_{\text{H}} \approx 1.5 \times 10^{23} \text{ cm}^{-2}$ , and  $N_{\text{H}} \approx 5 \times 10^{24} \text{ cm}^{-2}$ , respectively) was able to reproduce all the primary spectral lines and continuum shape around the Compton hump. In this best-fit multi-component reflector model, the higher  $N_{\text{H}}$  components contribute flux primarily to the Compton hump above 10 keV, while the lower  $N_{\text{H}}$  nuclear reflector is needed to reproduce the curvature of the continuum around 10 keV and provide the missing Fe line flux to model the whole structure with solar (as opposed to highly supersolar) metallicity. This configuration effectively decouples the two key features of Compton reflection, which are typically assumed to be coupled.
5. There are strong differences in the ratios of the 2–10 keV fluxes of the warm and cold reflection components, depending on the model employed and the parameters being fit. Because of the decoupling mentioned above, it could be dangerous to extrapolate the full properties of the reflector using simple reflection models, as has typically been done in the past with either lower-quality data or in type 1 AGNs diluted by transmitted continuum. We note that this decoupling could be at least partially responsible for some of the apparently high Fe abundances that have been quoted in the literature (e.g., M04).
6. Considering only the *Chandra* data, we find that  $\approx 30\%$  of the neutral Fe  $K\alpha$  line flux arises from  $>2''$  ( $\approx 140$  pc) in an extended configuration. Extrapolating this fraction inward assuming an increasing solid angle of dense molecular clouds implies that a significant fraction (and perhaps the majority) of the Fe  $K\alpha$  line arises from Compton scattering off material that is well outside the fiducial 1–10 pc torus material. A follow-up investigation looking into the spatial distribution of this material around several local AGN will be presented in F. E. Bauer et al. (2015, in preparation).
7. The multi-component reflector configuration envisioned here comprises a compact Compton-thick torus-like structure covering 50% of the sky and more tenuous, extended  $N_{\text{H}} \approx 10^{23} \text{ cm}^{-2}$  clouds covering  $\approx 13\%$  of the sky within the nuclear region ( $<140$  pc), as well as larger-scale, low-covering factor Compton-thick clouds, which extend out to 100s of pc. This scenario bears striking similarities to the multiple dust structures found via mid-IR interferometry for NGC 1068, and may eventually allow some independent corroboration of the clumpy torus model.

The benefits of combining high-quality  $>10$  keV spectral sensitivity from *NuSTAR* and spatially resolved spectroscopy from *Chandra* are clear, and could offer novel constraints on the few dozen closest, brightest AGN on the sky. Moving on to fainter and more distant objects, however, is likely to be challenging with current instrumentation, due to the extremely long integrations required and the increasingly poor intrinsic spatial resolutions obtained. Moreover, we should caution that our best-fit multi-component reflector, which we modeled only with three distinct column densities, could be an oversimplification, and in fact there might be a continuous distribution of different column density reflectors, given that the Galactic molecular cloud probability distribution function is well represented by a power law over a wide range of column densities (e.g., Lada et al. 1999; Goodman et al. 2009; Lombardi et al. 2010). Each cloud might contribute something to the overall reflection spectrum, thereby modifying the spectral shape away from that of a single monolithic reflector. Hopefully by acquiring similar constraints in other nearby Compton-thick AGN to those found for NGC 1068 and Circinus, combined with an assessment of the parameter space for obscuring clouds from mid-IR interferometry studies, we can amass enough clues in the short term to model distant and/or faint objects in a more informed manner. Ultimately, if the *Athena* mission (Nandra et al. 2013) can achieve its best-case scenario for spatial resolution of a few arcseconds, it could open up spatially resolved Fe analysis to a significantly larger range of AGN and help us place these local AGN in broader context.

We thank the anonymous referee for useful comments, which improved the clarity of the paper. We acknowledge financial support from the following: CONICYT-Chile Basal-CATA PFB-06/2007 (FEB, ET), FONDECYT grants 1141218 (FEB), 1140304 (PA), 1120061 (ET), and Anillo grant ACT1101 (FEB, PA, ET); Project IC120009 “Millennium Institute of Astrophysics (MAS)” funded by the Iniciativa Científica Milenio del Ministerio de Economía, Fomento y Turismo (FEB); Swiss National Science Foundation through the Ambizione fellowship grant PZ00P2\_154799/1 (MK); *NuSTAR* subcontract 44A-1092750 NASA ADP grant NNX10AC99G (WNB, BL); ASI/INAF grant I/037/12/0–011/13 (SP, AC, AM and GM); and STFC grant ST/J003697/1 (PG). This work was supported under NASA Contract No. NNG08FD60C, and made use of data from the *NuSTAR* mission, a project led by the California Institute of Technology, managed by the Jet Propulsion Laboratory, and funded by the National Aeronautics and Space Administration. We thank the *NuSTAR* Operations, Software and Calibration teams for support with the execution and analysis of these observations. This research has made use of the *NuSTAR* Data

Analysis Software (NuSTARDAS) jointly developed by the ASI Science Data Center (ASDC, Italy) and the California Institute of Technology (USA). This research has made use of data obtained through the High Energy Astrophysics Science Archive Research Center (HEASARC) Online Service, provided by the NASA/Goddard Space Flight Center.

*Facilities:* CXO (ACIS, HETG), XMM (pn, MOS), NuSTAR (FPMA, FPMB), Swift (XRT, BAT), BeppoSAX (MECS, PDS), Suzaku (XIS, PIN),

## REFERENCES

- Alonso-Herrero, A., Ramos Almeida, C., Mason, R., et al. 2011, *ApJ*, **736**, 82
- Antonucci, R. 1993, *ARA&A*, **31**, 473
- Antonucci, R. R. J., & Miller, J. S. 1985, *ApJ*, **297**, 621
- Arévalo, P., Bauer, F. E., Puccetti, S., et al. 2014, *ApJ*, **791**, 81
- Arévalo, P., Churazov, E., Zhuravleva, I., Hernández-Monteaquedo, C., & Revnivtsev, M. 2012, *MNRAS*, **426**, 1793
- Arnau, K. A. 1996, in ASP Conf. Ser., Vol. 101, *Astronomical Data Analysis Software and Systems*, ed. G. H. Jacoby & J. Barnes (San Francisco, CA: ASP), 17
- Bachetti, M., Rana, V., Walton, D. J., et al. 2013, *ApJ*, **778**, 163
- Bally, J., Stark, A. A., Wilson, R. W., & Henkel, C. 1988, *ApJ*, **324**, 223
- Baloković, M., Comastri, A., Harrison, F. A., et al. 2014, *ApJ*, **794**, 111
- Baumgartner, W. H., Tueller, J., Markwardt, C. B., et al. 2013, *ApJS*, **207**, 19
- Bock, J. J., Neugebauer, G., Matthews, K., et al. 2000, *AJ*, **120**, 2904
- Boldt, E. 1987, *PhR*, **146**, 215
- Brightman, M., Baloković, M., Stern, D., et al. 2015, *ApJ*, **805**, 41
- Brightman, M., & Nandra, K. 2011, *MNRAS*, **413**, 1206
- Brightman, M., Silverman, J. D., Mainieri, V., et al. 2013, *MNRAS*, **433**, 2485
- Brinkman, A. C., Kaastra, J. S., van der Meer, R. L. J., et al. 2002, *A&A*, **396**, 761
- Canizares, C. R., Huenemoerder, D. P., Davis, D. S., et al. 2000, *ApJL*, **539**, L41
- Capetti, A., Axon, D. J., & Macchetto, F. D. 1997, *ApJ*, **487**, 560
- Cecil, G., Bland, J., & Tully, R. B. 1990, *ApJ*, **355**, 70
- Cecil, G., Dopita, M. A., Groves, B., et al. 2002, *ApJ*, **568**, 627
- Crenshaw, D. M., & Kraemer, S. B. 2000, *ApJL*, **532**, L101
- Dauser, T., García, J., Wilms, J., et al. 2013, *MNRAS*, **430**, 1694
- Del Moro, A., Mullaney, J. R., Alexander, D. M., et al. 2014, *ApJ*, **786**, 16
- Dopita, M. A., Groves, B. A., Sutherland, R. S., Binette, L., & Cecil, G. 2002, *ApJ*, **572**, 753
- Elitzur, M., & Shlosman, I. 2006, *ApJL*, **648**, L101
- Evans, I. N., Ford, H. C., Kinney, A. L., et al. 1991, *ApJL*, **369**, L27
- Fabian, A. C., Kara, E., Walton, D. J., et al. 2013, *MNRAS*, **429**, 2917
- Fabian, A. C., Zoghbi, A., Ross, R. R., et al. 2009, *Natur*, **459**, 540
- Fanali, R., Caccianiga, A., Severgnini, P., et al. 2013, *MNRAS*, **433**, 648
- Gallimore, J. F., Baum, S. A., & O’Dea, C. P. 2004, *ApJ*, **613**, 794
- Gallimore, J. F., Baum, S. A., O’Dea, C. P., & Pedlar, A. 1996, *ApJ*, **458**, 136
- Gandhi, P., Horst, H., Smette, A., et al. 2009, *A&A*, **502**, 457
- Gandhi, P., Lansbury, G. B., Alexander, D. M., et al. 2014, *ApJ*, **792**, 117
- García, J., Dauser, T., Lohfink, A., et al. 2014, *ApJ*, **782**, 76
- Garmire, G. P., Bautz, M. W., Ford, P. G., Nousek, J. A., & Ricker, G. R. 2003, *Proc. SPIE*, **4851**, 28
- Gehrels, N., Chincarini, G., Giommi, P., et al. 2004, *ApJ*, **611**, 1005
- George, I. M., & Fabian, A. C. 1991, *MNRAS*, **249**, 352
- George, I. M., Turner, T. J., Yaqoob, T., et al. 2000, *ApJ*, **531**, 52
- Goodman, A. A., Pineda, J. E., & Schnee, S. L. 2009, *ApJ*, **692**, 91
- Grandi, P., Guainazzi, M., Mineo, T., et al. 1997, *A&A*, **325**, L17
- Greenhill, L. J., Gwinn, C. R., Antonucci, R., & Barvainis, R. 1996, *ApJL*, **472**, L21
- Groves, B. A., Cecil, G., Ferruit, P., & Dopita, M. A. 2004, *ApJ*, **611**, 786
- Guainazzi, M., Matt, G., Antonelli, L. A., et al. 1999, *MNRAS*, **310**, 10
- Guainazzi, M., Molendi, S., Vignati, P., Matt, G., & Iwasawa, K. 2000, *NewA*, **5**, 235
- Harrison, F. A., Craig, W. W., Christensen, F. E., et al. 2013, *ApJ*, **770**, 103
- Huchra, J. P., Vogeley, M. S., & Geller, M. J. 1999, *ApJS*, **121**, 287
- Iwasawa, K., Fabian, A. C., & Matt, G. 1997, *MNRAS*, **289**, 443
- Jaffe, W., Meisenheimer, K., Röttgering, H. J. A., et al. 2004, *Natur*, **429**, 47
- Jansen, F., Lumb, D., Altieri, B., et al. 2001, *A&A*, **365**, L1
- Kalberla, P. M. W., Burton, W. B., Hartmann, D., et al. 2005, *A&A*, **440**, 775
- Kallman, T., Evans, D. A., Marshall, H., et al. 2014, *ApJ*, **780**, 121
- Kaspi, S., Brandt, W. N., George, I. M., et al. 2002, *ApJ*, **574**, 643
- Kinkhabwala, A., Sako, M., Behar, E., et al. 2002, *ApJ*, **575**, 732
- Koshida, S., Minezaki, T., Yoshii, Y., et al. 2014, *ApJ*, **788**, 159
- Kraemer, S. B., & Crenshaw, D. M. 2000, *ApJ*, **544**, 763
- Kraemer, S. B., Ruiz, J. R., & Crenshaw, D. M. 1998, *ApJ*, **508**, 232
- Kraemer, S. B., Sharma, N., Turner, T. J., George, I. M., & Crenshaw, D. M. 2015, *ApJ*, **798**, 53
- Krolik, J. H., & Kriss, G. A. 1995, *ApJ*, **447**, 512
- Kuo, C. Y., Braatz, J. A., Condon, J. J., et al. 2011, *ApJ*, **727**, 20
- Lada, C. J., Alves, J., & Lada, E. A. 1999, *ApJ*, **512**, 250
- Lansbury, G. B., Alexander, D. M., Del Moro, A., et al. 2014, *ApJ*, **785**, 17
- Lightman, A. P., & White, T. R. 1988, *ApJ*, **335**, 57
- Lodato, G., & Bertin, G. 2003, *A&A*, **398**, 517
- Lombardi, M., Lada, C. J., & Alves, J. 2010, *A&A*, **512**, A67
- López-Gonzaga, N., Jaffe, W., Burtscher, L., Tristram, K. R. W., & Meisenheimer, K. 2014, *A&A*, **565**, A71
- Macchetto, F., Capetti, A., Sparks, W. B., Axon, D. J., & Boksenberg, A. 1994, *ApJL*, **435**, L15
- Madsen, K. K., Reynolds, S., Harrison, F., et al. 2015, *ApJ*, **801**, 66
- Magdziarz, P., & Zdziarski, A. A. 1995, *MNRAS*, **273**, 837
- Markowitz, A., Edelson, R., Vaughan, S., et al. 2003, *ApJ*, **593**, 96
- Markowitz, A., Papadakis, I., Arévalo, P., et al. 2007, *ApJ*, **656**, 116
- Markowitz, A., Reeves, J. N., George, I. M., et al. 2009, *ApJ*, **691**, 922
- Marshall, H. L. 2012, *Proc. SPIE*, **8443**, 1
- Martins, L. P., Rodríguez-Ardila, A., de Souza, R., & Gruenwald, R. 2010, *MNRAS*, **406**, 2168
- Matt, G., Bianchi, S., Guainazzi, M., & Molendi, S. 2004, *A&A*, **414**, 155
- Matt, G., Fabian, A. C., Guainazzi, M., et al. 2000, *MNRAS*, **318**, 173
- Matt, G., Guainazzi, M., Frontera, F., et al. 1997, *A&A*, **325**, L13
- McHardy, I. M., Gunn, K. F., Uttley, P., & Goad, M. R. 2005, *MNRAS*, **359**, 1469
- McHardy, I. M., Koerding, E., Knigge, C., Uttley, P., & Fender, R. P. 2006, *Natur*, **444**, 730
- McHardy, I. M., Papadakis, I. E., Uttley, P., Page, M. J., & Mason, K. O. 2004, *MNRAS*, **348**, 783
- Miller, J. S., Goodrich, R. W., & Mathews, W. G. 1991, *ApJ*, **378**, 47
- Molinari, S., Bally, J., Noriega-Crespo, A., et al. 2011, *ApJL*, **735**, L33
- Murphy, K. D., & Yaqoob, T. 2009, *MNRAS*, **397**, 1549
- Nandra, K., Barret, D., Barcons, X., et al. 2013, arXiv:1306.2307
- Nandra, K., O’Neill, P. M., George, I. M., & Reeves, J. N. 2007, *MNRAS*, **382**, 194
- Neškova, M., Sirocky, M. M., Nikutta, R., Ivezić, Ž., & Elitzur, M. 2008, *ApJ*, **685**, 160
- Nevalainen, J., David, L., & Guainazzi, M. 2010, *A&A*, **523**, A22
- Ogle, P. M., Brookings, T., Canizares, C. R., Lee, J. C., & Marshall, H. L. 2003, *A&A*, **402**, 849
- Oliva, E., Marconi, A., Maiolino, R., et al. 2001, *A&A*, **369**, L5
- Parker, M. L., Wilkins, D. R., Fabian, A. C., et al. 2014, *MNRAS*, **443**, 1723
- Perri, M., Puccetti, S., Spagnuolo, N., et al. 2014, *The NuSTAR Data Analysis Software Guide*, [http://heasarc.gsfc.nasa.gov/docs/nustar/analysis/nustar\\_swguide.pdf](http://heasarc.gsfc.nasa.gov/docs/nustar/analysis/nustar_swguide.pdf), v1.7 ed.
- Petrucci, P. O., Haardt, F., Maraschi, L., et al. 2001, *ApJ*, **556**, 716
- Pound, M. W. 1998, *ApJL*, **493**, L113
- Raban, D., Jaffe, W., Röttgering, H., Meisenheimer, K., & Tristram, K. R. W. 2009, *MNRAS*, **394**, 1325
- Ramos Almeida, C., Levenson, N. A., Rodríguez Espinosa, J. M., et al. 2009, *ApJ*, **702**, 1127
- Rana, V., Harrison, F. A., Bachetti, M., et al. 2015, *ApJ*, **799**, 121
- Reeves, J. N., & Turner, M. J. L. 2000, *MNRAS*, **316**, 234
- Risaliti, G., Miniutti, G., Elvis, M., et al. 2009, *ApJ*, **696**, 160
- Ross, R. R., & Fabian, A. C. 2005, *MNRAS*, **358**, 211
- Schartmann, M., Burkert, A., Krause, M., et al. 2010, *MNRAS*, **403**, 1801
- Shemmer, O., Brandt, W. N., Netzer, H., Maiolino, R., & Kaspi, S. 2006, *ApJL*, **646**, L29
- Suganuma, M., Yoshii, Y., Kobayashi, Y., et al. 2006, *ApJ*, **639**, 46
- Swartz, D. A., Ghosh, K. K., Tennant, A. F., & Wu, K. 2004, *ApJS*, **154**, 519
- Tremblin, P., Schneider, N., Minier, V., et al. 2014, *A&A*, **564**, A106
- Tsujimoto, M., Guainazzi, M., Plucinsky, P. P., et al. 2011, *A&A*, **525**, A25
- Tully, R. B. 1988, *Nearby Galaxies Catalog* (Cambridge: Cambridge Univ. Press)
- Unger, S. W., Lewis, J. R., Pedlar, A., & Axon, D. J. 1992, *MNRAS*, **258**, 371
- Urry, C. M., & Padovani, P. 1995, *PASP*, **107**, 803
- Veilleux, S., Shopbell, P. L., Rupke, D. S., Bland-Hawthorn, J., & Cecil, G. 2003, *AJ*, **126**, 2185
- Verner, D. A., Ferland, G. J., Korista, K. T., & Yakovlev, D. G. 1996, *ApJ*, **465**, 487

- Walton, D. J., Fuerst, F., Harrison, F., et al. 2013, [ApJ](#), 779, 148
- Walton, D. J., Harrison, F. A., Grefenstette, B. W., et al. 2014, [ApJ](#), 793, 21
- Walton, D. J., Roberts, T. P., Mateos, S., & Heard, V. 2011, [MNRAS](#), 416, 1844
- Wik, D. R., Hornstrup, A., Molendi, S., et al. 2014, [ApJ](#), 792, 48
- Wilms, J., Allen, A., & McCray, R. 2000, [ApJ](#), 542, 914
- Wilson, A. S., & Ulvestad, J. S. 1987, [ApJ](#), 319, 105
- Wise, M. W., Huenemoerder, D. P., & Davis, J. E. 1997, in ASP Conf. Ser. 125, *Astronomical Data Analysis Software and Systems VI*, ed. G. Hunt & H. Payne (San Francisco, CA: ASP), 477
- Woo, J.-H., & Urry, C. M. 2002, [ApJ](#), 579, 530
- Yaqoob, T. 2012, [MNRAS](#), 423, 3360
- Yaqoob, T., & Padmanabhan, U. 2004, [ApJ](#), 604, 63
- Young, A. J., Wilson, A. S., & Shopbell, P. L. 2001, [ApJ](#), 556, 6